

Responses to Anonymous Referee #2's comments (RC2):

Thanks are extended to the Professor, Markku Kulmala, and to the two anonymous Referees, for their careful work and thoughtful and very important suggestions that greatly improve the manuscript.

The following text contains the Referees' comments (black), our replies (blue) and the changes made to the manuscript (red).

Comment 01: The authors used the empirical mode decomposition (EMD) to capture the time varying features in the measured 3D E-filed data. Similar tools also exist, such as the wavelet transformation. Why the authors chose EMD over the wavelet method? EMD is known to likely cause problems at the beginning and end of a time series. How did the authors deal with such issues? The application of EMD is also vulnerable to mode mixing. How was this problem handled in estimating the time-varying mean values?

Response:

As you pointed out that the EMD method in the original manuscript (MS) may cause the ending effects and mode mixing. In order to solve these issues, we use the discrete wavelet transform (DWT) (Daubechies, 1990) and the ensemble empirical mode decomposition (EEMD) methods (Wu and Huang, 2009) to extract the meaningful time-varying means over the approximately 17-min timescales, because these two methods can significantly reduce the ending effects and mode mixing (please see the references of Daubechies, 1990 and Wu and Huang, 2009 for details).

As shown in the revised MS, the 17-min time-varying means can be defined as the 10-th order approximation component of DWT or the summation of the last four EEMD component and the residual.

According to your suggestion, the following changes have been made in the revised MS:

“... Here, we use the discrete wavelet transform (DWT) method (Daubechies, 1990) and the ensemble empirical mode decomposition (EEMD) method (Wu and

Huang, 2009), which are widely used in various geophysical studies (e.g. Grinsted et al., 2004; Huang and Wu, 2008; Wu et al., 2011), to estimate the time-varying mean values of the measured non-stationary 3-D E-field data. We select these two methods since the DWT with higher orders of Daubechies wavelet (e.g. db10) and the EEMD can extract a reasonable and physically meaningful time-varying mean (Su et al., 2015). Each step for revealing the 3-D E-field pattern is described in detail as follows:

The DWT uses a set of mutually orthogonal wavelet basis functions, which are dilated, translated and scaled versions of a mother wavelet, to decompose an E-field series $E(t, z)$ into a series of successive octave band components (Percival and Walden, 2000), i.e.,

$$E(t, z) = \sum_{i=1}^N \psi_i(t, z) + \chi_N(t, z) \quad (1)$$

Where N is the total number of decomposition levels, $\psi_i(t, z)$ denotes the i -th level wavelet detail component, and $\chi_N(t, z)$ represents the N -th level wavelet approximation (or smooth) component. As N increases, the frequency contents become lower and thus the N -th level approximation component could be regarded as the time-varying mean values (e.g. Percival and Walden, 2000; Su et al., 2015). In this study, the DWT decomposition is performed with the Daubechies wavelet of order 10 (db10) at level 10, and thus the 10-th order approximation component can be defined as the time-varying mean:

$$\bar{E}(t, z) = \chi_{10}(t, z) \quad (2)$$

which reflect the averages of the $E(t, z)$ series over a scale of 2^{10} s (about 17.1 minutes).

On the other hand, according to the empirical mode decomposition (EMD) method, the time series $E(t, z)$ can be decomposed as (Huang et al., 1998)

$$E(t, z) = \sum_{i=1}^N \xi_i(t, z) + \eta_N(t, z) \quad (3)$$

through a sifting process, where $\xi_i(t, z)$ ($i = 1, 2, \dots, N$) are the intrinsic mode functions (IMFs), and $\eta_N(t, z)$ is a residual (which is the overall trend or mean). To reduce the end effects and mode mixing in EMD, the EEMD method is proposed by Wu and Huang (2009). In EEMD, a set of white noise series, $w_j(t, z)$ ($j = 1, 2, \dots, N_e$), are added to the original signal $E(t, z)$. Then, each noise-added series is decomposed into IMFs followed by the same sifting process as in EMD. Finally, the i -th EEMD component is defined as the ensemble mean of the i -th IMFs of the total of N_e noise-added series (see Wu and Huang, 2009 for details).

In this study, the time-varying mean values $\bar{E}(t, z)$ can be alternatively defined as the sum of the last four EEMD components, $\xi_{10}(t, z)$ to $\xi_{13}(t, z)$, and the residual, $\eta_{13}(t, z)$, i.e.

$$\bar{E}(t, z) = \sum_{i=10}^{13} \xi_i(t, z) + \eta_{13}(t, z) \quad (4)$$

which is approximately the 17.3 minutes (very close to the timescale of ~ 17.1 minutes used in DWT) or longer timescale variability trend (Wu et al., 2011), because the maximum mean frequency of the last four EEMD components is 5.78×10^{-2} Hz (see Figs. S5 and S6 in the Supplement for details).

According to the above definitions, the time-varying mean can be obtained by the DWT and EEMD methods over the timescale of about 17 minutes. As an example, Fig. 2 shows the results of db10 DWT analysis (Fig. 2b) and EEMD decompositions (Fig. 2c) for an E-field time series $E(t, z)$ in our field campaign. It can be seen that DWT and EEMD can properly capture the time-varying mean over the timescale of 17 minutes, with very little difference between the two methods." [Please see pages 6-8 in the](#)

revised MS for details.

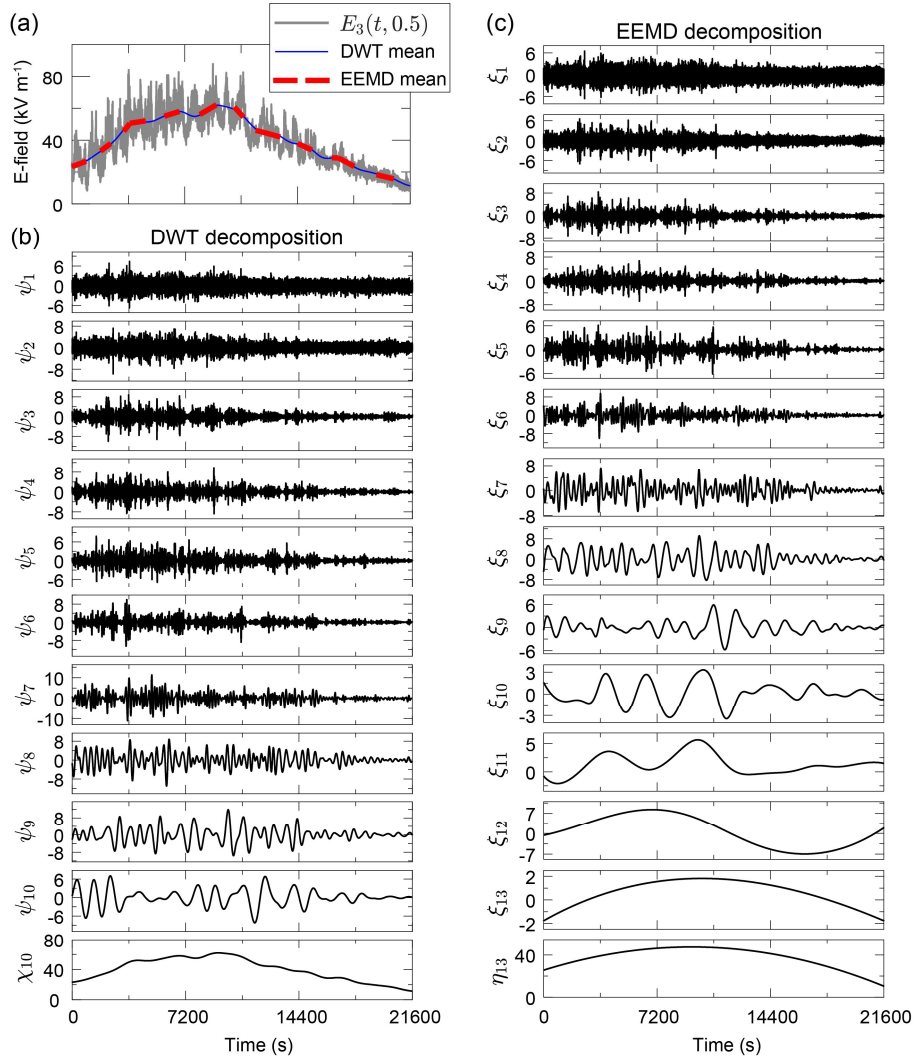


Figure 2. The resulting DWT and EEMD components from a measured vertical E-field component at 0.5 m height, $E_3(t, 0.5)$, with a total of $N_d=21600$ data points. (a) shows the original E-field time series (gray line), and the time-varying mean obtained by DWT (red line) and EEMD (blue dashed line). (b) shows the detailed components ψ_1 - ψ_{10} and approximation component χ_{10} of DWT. (c) shows the EEMD components ξ_1 - ξ_{13} and the residue η_{13} . In the EEMD, N is specified as $\log_2(N_d) - 1$, the member of ensemble N_e is 100, and the added white noise in each ensemble member has a standard deviation of 0.2. Times are shown relative to May 6, 2014 at 13:00:00 UTC+8.

Please see page 37 lines2-11 in the revised MS for details.

Additionally, in supplementary materials, the following changes have been made in the revised Supplement:

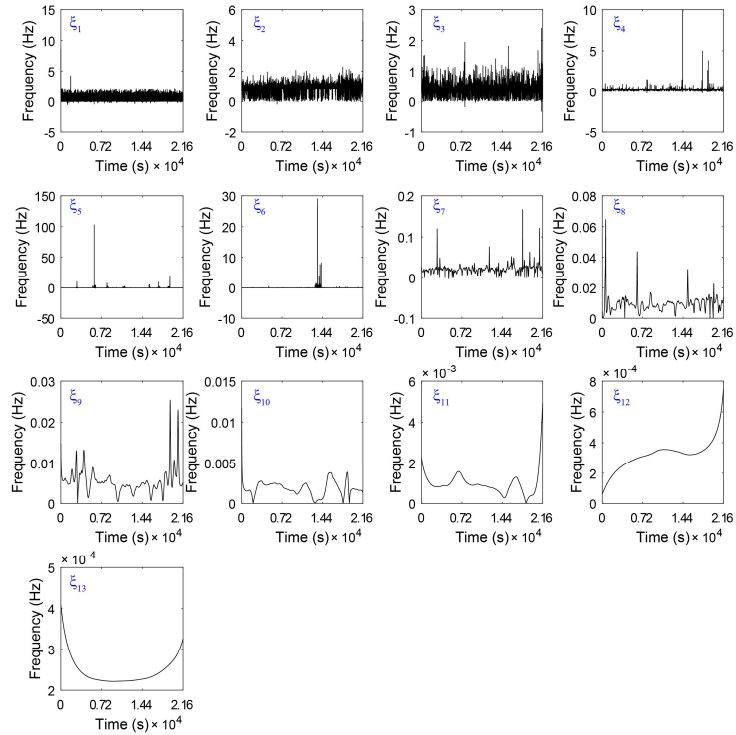


Figure S5. The instantaneous frequency of the EEMD components ξ_1 - ξ_{13} for the vertical E-field series at 0.5 m height, i.e. $E_3(0.5)$.

Please see page 9 in the revised Supplement for details.

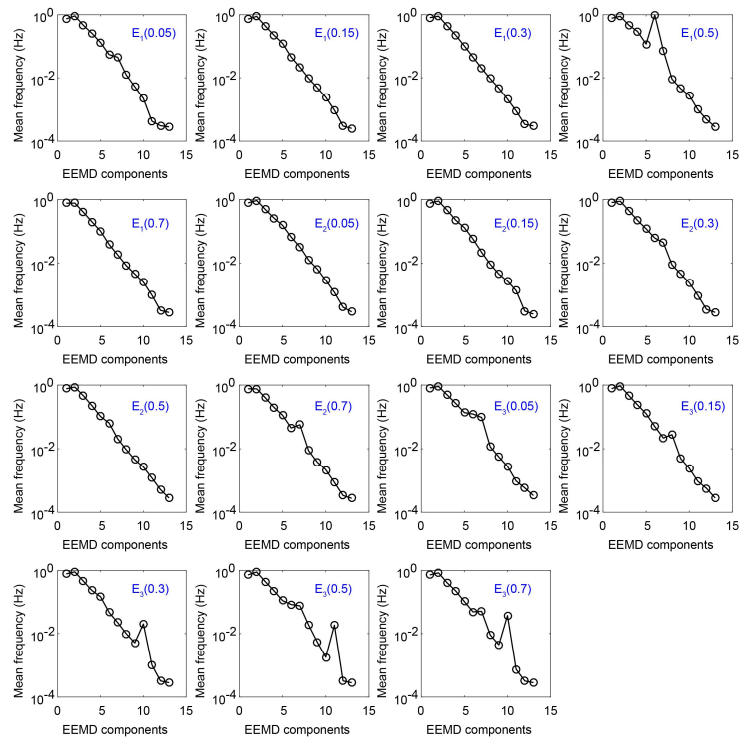


Figure S6. The mean frequencies of IMFs ξ_1 - ξ_{13} for 3-D E-fields at all measurement points, $E_1 - E_3$ from 0.05 to 0.7 m height.

Please see page 10 in the revised Supplement for details.

Comments 02: a) The reduction of height z to the dimensionless z^* is dependent on the saltation height, which is determined from measured SPC-91 data. I understood that SPC-91 is a particle counter that gives number size distribution. How was the mass information obtained from this data? What assumptions you made? How do the measurement uncertainties and assumptions influence the estimated saltation height? Does the saltation height vary with time?

b) It is described in section 4.1 that ‘normalized vertical component $E3^*$ increases monotonically as height increases in the saltation layer’. However, in fig. 5c, the data points clustering at z^* between 0.5 and 1 showed lower $E3^*$ than the ones at smaller z^* . Therefore, this statement is not valid. It also seems that data points at $z^*=1-1.5$ are always deviated from the trends in Figs. 5a-c. What could be the reason?

c) The authors used hourly bins in Fig. 5. How will the patterns look like if finer bins are used, e.g. 30 min or 10 min?

Response:

Our responses for this comment are threefold:

a) In fact, the SPC measures the particle number passing through the measurement area per second in the range of 30-490 μm with 64 bins, as shown in Fig. R1. That is to say, it measures the particle number flux with 64 given bins. If the particle mass density is known, we can estimate the mass flux based on the SPC data (please see Text S1 in the Supplement for details). The detailed estimation of mass flux from SPC data can be also found in the following reference:

“Mikami, M., Yamada, Y., Ishizuka, M., Ishimaru, T., Gao, W., & Zeng, F. (2005). Measurement of saltation process over gobi and sand dunes in the Taklimakan desert, China, with newly developed sand particle counter. *Journal of Geophysical Research: Atmospheres*, 110(D18).”

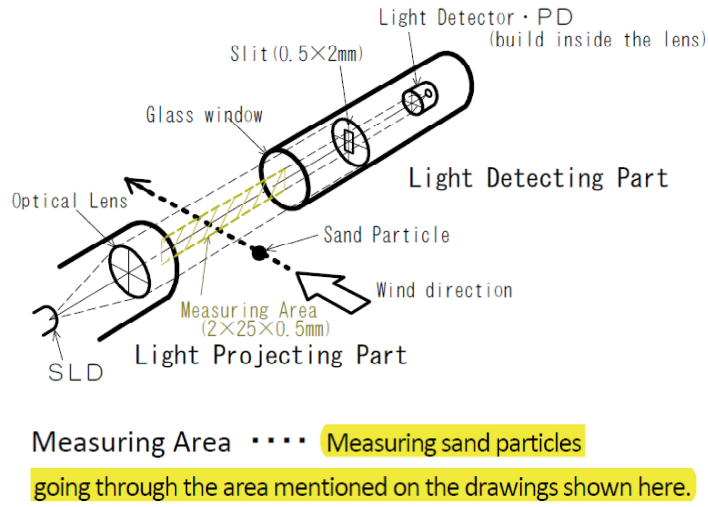


Figure R1. Schematic diagram of the measuring principle of SPC-91, which is redraw based on the “SPC-91 Installation Guide, Niigata Electric Co., Ltd.”

Because SPC measures the particle diameter with uncertainty of $\Delta d = \pm 0.015$ mm (SPC-91 Installation Guide, Niigata Electric Co., Ltd.), the uncertainty of estimating mass flux is $\Delta q \sim 3d^2\Delta d$ (i.e. $q \sim d^3 \Rightarrow \Delta q \sim 3d^2\Delta d$). The measured mass flux profiles are shown in Fig. S2 (see below). As discussed in the Text S1 in the Supplement, the saltation height can be approximated as a function of the fitted parameter a :

$$z_{salt} = -\frac{\ln(0.01)}{a} \quad (R1)$$

where the measured mass flux profile is excellently fitted by the exponential function $q(z) = q_0 \exp(-az)$.

According to Eq. R1, the uncertainty of z_{salt} can be estimated as:

$$\Delta z_{salt} = \frac{\ln(0.01)}{a^2} \Delta a \quad (R2)$$

where Δa is the 95% confidence bounds.

It is worth noting that in the revised MS, mass flux q is estimated over every 30-

min time intervals, in order to collect sufficient sand sample and capture the full range of turbulent fluctuations (see Martin and Kok, 2017 and Sherman and Li, 2012 for the details). Fig. S3 shows the comparison of the mass flux and z_{salt} estimated by three different time intervals. It can be seen that there is no obvious difference between the mean values but the standard deviation decreases with increasing time interval. Fig. S3 shows the estimated saltation height. We can see that z_{salt} slightly varies with time and can be approximately considered as a constant, which is also verified in the previous studies in the case of steady-state saltation (Kok et al., 2012; Martin and Kok, 2017). In the revised MS, the height z is normalized by the mean saltation height \bar{z}_{salt} , because it could obtain a better representation of the E-field profiles (Fig. 5 in the revised MS).

For comments 02 a), the following changes have been made in the revised Supplement:

“...In our field campaign, we measured the saltating particle number flux at 6 heights from 0.05 to 0.7 m. Thus, the mass flux at each measurement height can be reasonably estimated by

$$q(z) = \frac{\pi\rho_p}{6L_xL_yT_w} \sum_{i=1}^n (N_i d_i^3) \quad (s2)$$

Note that the summation \sum is performed for the particles located in the range of $[z, z + \Delta z]$ over the 30-min time windows (i.e., $T_w=30$ minutes), in order to collect sufficient sand samples and capture the full range of turbulent fluctuations (e.g. Martin and Kok, 2017; Sherman and Li, 2012). Since SPC-91 measures the particle diameter with an uncertainty of $\Delta d = \pm 0.015$ mm (see SPC-91 Installation Guide, Niigata Electric Co., Ltd. for details), the uncertainty of estimating mass flux is $\Delta q \sim 3d^2\Delta d$ (i.e. $q \sim d^3 \Rightarrow \Delta q \sim 3d^2\Delta d$). As shown in Fig. S2, the measured mass flux data during different time intervals can be well fitted by the exponential functions (Shao, 2008):

$$q(z) = q_0 \exp(-az) \quad (s3)$$

where q_0 is the value of q at $z = 0$ and a is a positive empirical constant. Hence, the total mass flux can be determined by

$$Q = \int_0^{+\infty} q(z) dz = \frac{q_0}{a} \quad (s4)$$

Similarly, the uncertainty of the total mass flux is

$$\Delta Q = \frac{a\Delta q_0 - q_0\Delta a}{a^2} \quad (s5)$$

Additionally, the saltation height, which is defined as the height below which 99 % of the total mass flux is present, can be given by (Dupont et al., 2013; Kok et al., 2012)

$$\int_0^{z_{salt}} q(z) dz = \frac{0.99q_0}{a} \quad (s6a)$$

$$\Rightarrow z_{salt} = -\frac{\ln(0.01)}{a} \quad (s6b)$$

Similarly, the uncertainty of the saltation height is

$$\Delta z_{salt} = -\frac{\ln(0.01)}{a^2} \Delta a \quad (s7)$$

As shown in Fig. S3, the estimated saltation height slightly varies with time, and thus we use the mean saltation height, which is 0.172 ± 0.0343 m, to obtain the dimensionless height z^+ . For different time windows (i.e. $T_w = 5, 10, 30$ minutes), there is no obvious differences between the mean values of Q and z_{salt} , but the

standard deviations decrease as T_w increases (Fig. S3). Please see pages 2-4 in the revised Supplement for details.

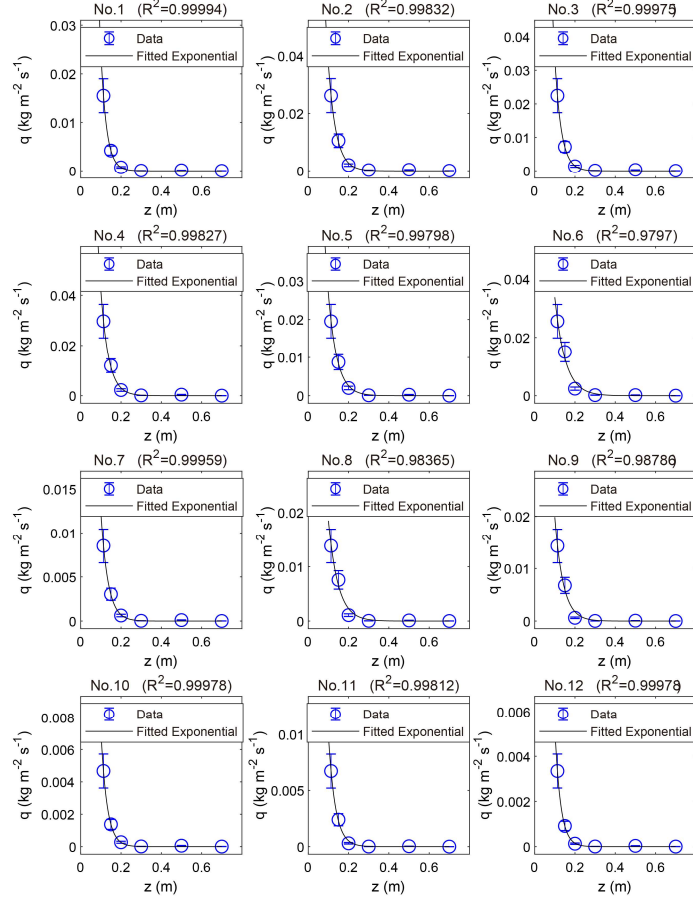


Figure S2. An example of the estimation of the total mass flux Q and saltation height z_{salt} in this study, where No. i corresponds to time interval of $[(i - 1)T, iT]$. The measured mass flux data are fitted by the exponential function $q(z) = q_0 \exp(-az)$, with R^2 larger than 0.9. Thus, the total mass flux and saltation height can be estimated by Eqs. s4-s7 in the Supplement, respectively. Please see page 6 in the revised Supplement for details.

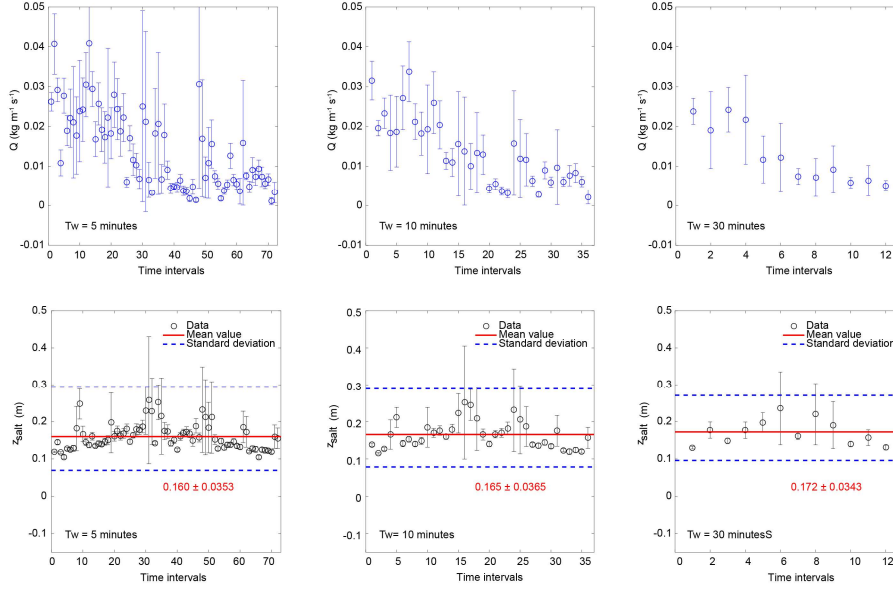


Figure S3. The estimated total mass flux Q (upper panels) and the saltation height z_{salt} (lower panels) with different time windows T_w (i.e. 5, 10, and 30 minutes) using the methods described in the Text S1. In the lower panels, the horizontal lines (in red) denote the mean saltation height, and the horizontal dashed lines (in blue) denote standard deviation. The shaded areas denote the relatively steady period of the observed dust storm.

Please see page 7 in the revised Supplement for details.

b) In the original MS, the heights z are normalized by z_{salt} in each time interval (1 h), thus leading to the data points at $z^*=1-1.5$ are always deviated from the trends. By contrast, in the revised MS, because the heights z are normalized by the mean saltation height \bar{z}_{salt} (a constant), these exist only five dimensionless heights z^+ (which, in turn, correspond to five measurement points) in Fig. 5. As shown in the Fig. R2 (redrawn from Figure 5 in the revised MS), at each measurement point, all data are horizontally distributed.

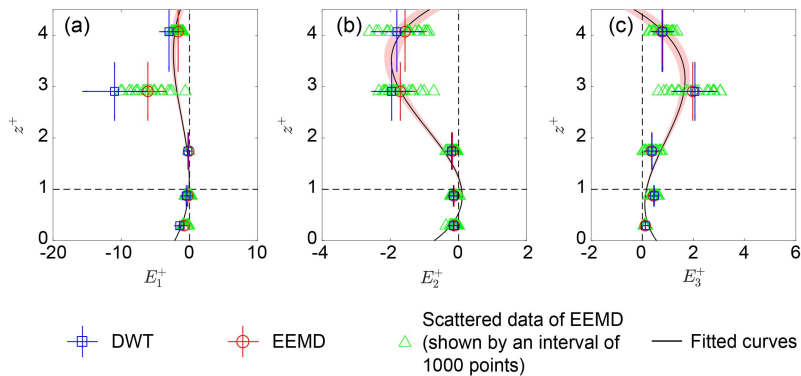


Figure R2 (redrawn from Figure 5 in the revised MS). Vertical profiles of the normalized 3-D E-field. Subgraphs (a)-(c), in turn, correspond to the vertical profiles of E_1^+ , E_2^+ , and E_3^+ of the observed dust storm. Squares and circles denote the DWT mean and EEMD mean values of the normalized E-field data, respectively. Triangles denote the scattered data of EEMD, which are shown by an interval of 1000 points (that is the first, 1001-th, 2001-th... points are shown). Error bars are standard deviations. Lines denote robust linear least-squares fitting of the normalized E-field data obtained by DWT and EEMD method using 3-order polynomials (with R^2 of 0.77, 0.78, and 0.93, respectively), where the shaded areas denote 95% confidence bounds.

In addition, from Fig. R2, we can see that the fitted vertical component curve decreases monotonically with increasing height when z^+ is less than 1. Therefore, in the revised MS, we have modified the statement of “normalized vertical component E_3^* increases monotonically as height increases in the saltation layer” as:

“... Interestingly, Fig. 5c shows that during dust storms, all normalized components, E_1^+ to E_3^+ , decreases monotonically as height increases in the saltation layer (i.e. $z^+ \leq 1$), similar to the pattern of vertical component in pure saltation...”

Please see page 19 lines 21-23 in the revised MS for details.

c) In the revised MS, when exploring the 3-D E-field pattern, we do not use time window (hourly bins in the original MS) to analyze E-field series. That is, for an E-field component at a given height [e.g. $E_3(t, 0.5)$ series], there are a total of 21,600 dimensionless E-field data points (i.e. all data points during 6 hours) E_3^+ used to fit the 3-order polynomial function, as shown in Fig. R2. Therefore, in the revised MS we do not explore (not required) the effects of time window (e.g. 10 or 30 minutes) on E-field pattern.

Comments 03: The authors considered midair particle-particle collisions with a viscoelastic force model in the saltation model to stimulate particle motion. This inclusion of the midair particle-particle interaction is shown to be important. However, during midair particle-particle interaction, particle diameters may change upon collision or frictional contact, e.g. due to cleavage of agglomerates, which may increase

the total number of particles in the system and shift the size and charge distributions of the particle population. Have the authors thought about these effects?

Response:

In our model, we do not consider particle agglomeration and fragmentation during collisions. According to your comment, we have added the discussions about particle agglomeration and fragmentation:

“However, a remaining critical challenge is still to simulate particle triboelectric charging in dust storms precisely. The driving atmospheric turbulent flows having a typical Reynolds number on the order of 10^8 cover a broad range of length and time scales, which needs huge computational cost to resolve (e.g. Shao, 2008). On the other hand, particle triboelectric charging is so sensitive to particle’s collisional dynamics that it needs to resolve each particle collisional dynamics (e.g. Hu et al., 2012; Lacks and Sankaran, 2011). To model the particle’s collisional dynamics properly, the time steps of DEM are generally from 10^{-7} to 10^{-4} s (Norouzi et al., 2016). However, steady-state saltation motion often requires several seconds to several tens of seconds to reach the equilibrium state. In this study, when $u_* = 0.5 \text{ m s}^{-1}$ and the computational domain is $0.5 \times 0.1 \times 1.0 \text{ m}^3$, the total number of saltating particles exceeds 7×10^4 (Fig. S8 in the Supplement). Consequently, the triboelectric charging in saltation is currently very difficult to simulate, where a large number of polydisperse sand particles, the high Reynolds-number turbulent flow, and the inter-particle electrostatic forces are mutually coupled. In the present version of the model, we do not consider the particle-particle interactions such as particle agglomeration and fragmentation during particle collision or frictional contact, as well as the particle-turbulence interaction that is the effects of turbulent fluctuations on the triboelectric charging and dynamics of particles. Further studies require considerable effort to incorporate these interactions, especially turbulence, which is very important for large wind velocity.” Please see page 25 lines 1-20 in the revised MS for details.

Comments 04: The authors performed a simple sensitivity study of mass flux on the

effects of E-field intensity factors. It is said that the red curve corresponds to the observed dust storm. Where did the authors obtain the intensity factors for the other two cases? Are they realistic compared to reported observations in literature?

Response:

In the original MS, λ is actually the height-averaged time-varying mean of the E-field $\langle \overline{E}_i \rangle$, which is clearly defined by Eq. 5 in the revised MS. To eliminate the ambiguous meaning of λ , we directly regard the height-averaged time-varying mean as a basic parameter in the revised MS (therefore λ has been removed). The determination of $\langle \overline{E}_i \rangle$ is clearly shown in section 2.2 of the revised MS, namely:

“... Here, we use the discrete wavelet transform (DWT) method (Daubechies, 1990) and the ensemble empirical mode decomposition (EEMD) method (Wu and Huang, 2009), which are widely used in various geophysical studies (e.g. Grinsted et al., 2004; Huang and Wu, 2008; Wu et al., 2011), to estimate the time-varying mean values of the measured non-stationary 3-D E-field data. We select these two methods since the DWT with higher orders of Daubechies wavelet (e.g. db10) and the EEMD can extract a reasonable and physically meaningful time-varying mean (Su et al., 2015). Each step for revealing the 3-D E-field pattern is described in detail as follows:

The DWT uses a set of mutually orthogonal wavelet basis functions, which are dilated, translated and scaled versions of a mother wavelet, to decompose an E-field series $E(t, z)$ into a series of successive octave band components (Percival and Walden, 2000), i.e.,

$$E(t, z) = \sum_{i=1}^N \psi_i(t, z) + \chi_N(t, z) \quad (1)$$

Where N is the total number of decomposition levels, $\psi_i(t, z)$ denotes the i -th level wavelet detail component, and $\chi_N(t, z)$ represents the N -th level wavelet approximation (or smooth) component. As N increases, the frequency contents become lower and thus the N -th level approximation component could be regarded

as the time-varying mean values (e.g. Percival and Walden, 2000; Su et al., 2015). In this study, the DWT decomposition is performed with the Daubechies wavelet of order 10 (db10) at level 10, and thus the 10-th order approximation component can be defined as the time-varying mean:

$$\bar{E}(t, z) = \chi_{10}(t, z) \quad (2)$$

which reflect the averages of the $E(t, z)$ series over a scale of 2^{10} s (about 17.1 minutes).

On the other hand, according to the empirical mode decomposition (EMD) method, the time series $E(t, z)$ can be decomposed as (Huang et al., 1998)

$$E(t, z) = \sum_{i=1}^N \xi_i(t, z) + \eta_N(t, z) \quad (3)$$

through a sifting process, where $\xi_i(t, z)$ ($i = 1, 2, \dots, N$) are the intrinsic mode functions (IMFs), and $\eta_N(t, z)$ is a residual (which is the overall trend or mean). To reduce the end effects and mode mixing in EMD, the EEMD method is proposed by Wu and Huang (2009). In EEMD, a set of white noise series, $w_j(t, z)$ ($j = 1, 2, \dots, N_e$), are added to the original signal $E(t, z)$. Then, each noise-added series is decomposed into IMFs followed by the same sifting process as in EMD. Finally, the i -th EEMD component is defined as the ensemble mean of the i -th IMFs of the total of N_e noise-added series (see Wu and Huang, 2009 for details).

In this study, the time-varying mean values $\bar{E}(t, z)$ can be alternatively defined as the sum of the last four EEMD components, $\xi_{10}(t, z)$ to $\xi_{13}(t, z)$, and the residual, $\eta_{13}(t, z)$, i.e.

$$\bar{E}(t, z) = \sum_{i=10}^{13} \xi_i(t, z) + \eta_{13}(t, z) \quad (4)$$

which is approximately the 17.3 minutes (very close to the timescale of ~17.1 minutes used in DWT) or longer timescale variability trend (Wu et al., 2011), because the maximum mean frequency of the last four EEMD components is 5.78×10^{-2} Hz (see Figs. S5 and S6 in the Supplement for details).

According to the above definitions, the time-varying mean can be obtained by the DWT and EEMD methods over the timescale of about 17 minutes. As an example, Fig. 2 shows the results of db10 DWT analysis (Fig. 2b) and EEMD decompositions (Fig. 2c) for an E-field time series $E(t, z)$ in our field campaign. It can be seen that DWT and EEMD can properly capture the time-varying mean over the timescale of 17 minutes, with very little difference between the two methods.

Since the 3-D E-field are measured at five heights in our field campaign, we thus define the height-averaged time-varying mean values as

$$\langle \overline{E}_i(t, z) \rangle = \left| \frac{1}{(0.7 - 0.05)} \int_{0.05}^{0.7} \overline{E}_i(t, z) dz \right| \quad (5)$$

in the range of 0.05 to 0.7 m height, in order to normalize the E-field data by a unified quantity....” Please see pages 6-8 in the revised MS for details.

Therefore, the height-averaged time-varying mean (i.e. intensity factors in the original MS) can be obtained by above methods. The height-averaged time-varying means of the observed dust storm are shown in Fig. S7 in the revised Supplement. So far, since there is no other multi-points measurement of 3-D E-field during dust storms, we cannot compare our results with other data in the literature.

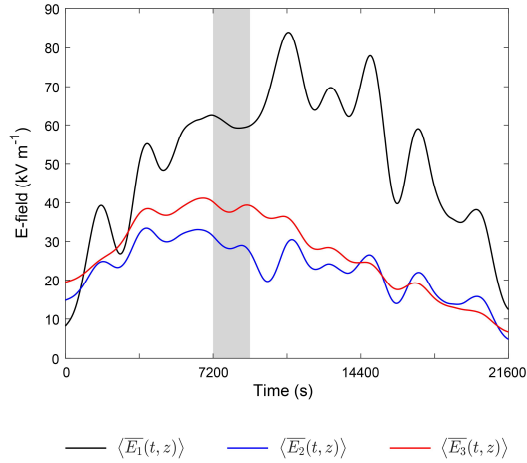


Figure S7. The height time-varying mean series of the 3-D E-field. The shaded area denotes the relatively steady period of the observed dust storms. Times are shown relative to May 6, 2014 at 13:00:00 UTC+8.

Please see page 11 in the revised Supplement for details.

Comments 05: This study is based on one case. It therefore lacks the statistics to reach statements, like ‘This 3-D E-field model successfully resolves the discrepancy between the 1-D E-field model (e.g. Kok and Renno, 2008) and the recent measurement (i.e. Esposito et al., 2016).’ or ‘The DEM implemented by cell-based algorithms is robust enough to detect and evaluate all particle-particle midair collisional dynamics.’ Two aspects here:

a) It is weak in reaching conclusions based on a single case study. Also for model validation purpose, it would be important to apply the algorithms to at least another case. It will largely improve the quality and strength of the results, if the authors could add a second case to support.

b) The 3-D E-field model indeed shows a good agreement with observations, but the discrepancy between the 1-D E-field model and measurement may not only be due to the exclusion of the two other dimensions of the E-field. It is good that the authors took into consideration of particle-particle midair collisional dynamics in the model, but what the authors implemented in the model certainly do not account for all. I would like to suggest the authors make a revision of the language in sections 5.3, 5.4

and 6 to avoid exaggeration in discussing the methods and results as well as conclusions drawn therefrom.

Response:

Unfortunately, we have only observed one dust storms in the 2014 field campaign since the occurrence of dust events are highly stochastic. As you pointed out that, the properties of dust storms may vary from event to event. Thus, in the revised MS, we have added the following discussions in section 5.1:

“...Additionally, the 3-D E-field pattern of dust storms may vary event to event, because it is strongly related to the driving mechanisms of dust storms, such as monsoon winds, squall lines, and thunderstorms (Shao, 2008), and ambient conditions, such as temperature and relative humidity (Esposito et al., 2016; Zhang and Zheng, 2018). Although the 3-D E-field pattern revealed in this study may not be a universal feature, the proposed E-field data analysis method can be easily applied to other cases.”
Please see page 23 lines 2-8 in the revised MS for details.

In addition, according to your suggestion, we have modified the language in sections 5.3, 5.4 and 6 in order to avoid exaggeration. The main reversion are as follows:

In section 5.3:

“... The DEM implemented by cell-based algorithms is effectively to detect and evaluate most of the particle-particle midair collisional dynamics (Norouzi et al., 2016) ...”

Please see page 24 lines 8-10 in the revised MS for details.

In section 5.4:

“...This 3-D E-field model may resolve the discrepancy between the 1-D E-field model (e.g. Kok and Renno, 2008) and the recent measurement (i.e. Esposito et al., 2016)...”

Please see page 24 lines 26-27 in the revised MS for details.

In section 6:

“(2) the inclusion of 3-D E-field in saltation model may resolve the discrepancy between previous 1-D E-field model (e.g. Kok and Renno, 2008) and measurements (Esposito et al., 2016) in the aspect of whether the E-field inhibits or enhances saltation...”

Please see page 26 lines 3-6 in the revised MS for the details.

Comments 06: P20 line 26: remove explicitly; 7. P20 line 28: It does not seem to me that the 3-order polynomial curves can capture the patterns well in Fig. 5. Therefore, it is inappropriate to say ‘... providing a detailed characterization...’

Response:

According to your suggestion, we have modified the statement “...we explicitly account for the particle-particle tribo-electrification during midair collisions in saltation...” as

“...we account for the particle-particle triboelectric charging during midair collisions in saltation...”

Please see page 24 lines 7-8 in the revised MS for details.

We have modified the statement “...providing a detailed characterization of the 3-D E-field during dust storms for the first time...” as

“...providing a simple representation of the 3-D E-field during dust storms for the first time...”

Please see page 26 lines 2-3 in the revised MS for details.

1 **Effects of three-dimensional electric field on saltation**
2 **during dust storms: An observational and numerical**
3 **study**

4

5 Huan Zhang¹, You-He Zhou^{1,*}

6

7 ¹Department of Mechanics and Engineering Science, College of Civil Engineering and
8 Mechanics, Lanzhou University, Key Laboratory of Mechanics on Disaster and
9 Environment in Western China, The Ministry of Education of China, Lanzhou 730000,
10 PR China.

11

12 *Correspondence to: You-He Zhou (zhouyh@lzu.edu.cn)

13

1 **Abstract.** Particle triboelectric charging being ubiquitous in nature and industry,
2 potentially plays a key role in dust events, including the lifting and transport of sand
3 and dust particles. However, the properties of the electric field (E-field) and its
4 influences on saltation during dust storms remain obscure as the high complexity of
5 dust storms and the existing numerical studies mainly limited to one-dimensional (1-
6 D) E-field. Here, we quantify the effects of real three-dimensional (3-D) E-field on
7 saltation, through a combination of field observations and numerical modelling. The
8 3-D E-fields in the sub-meter layer from 0.05 to 0.7 m above the ground during a dust
9 storm are measured at Qingtu Lake Observation Array site. [The time-varying mean of](#)
10 [E-field series over the timescales of about 17 minutes are extracted by the discrete](#)
11 [wavelet transform \(DWT\) and ensemble empirical mode decomposition \(EEMD\)](#)
12 [methods.](#) The measured results show that each component of the 3-D E-field data
13 [roughly](#) collapses on a single 3-order polynomial curve when normalized. Such 3-D E-
14 field data close to the ground within a few centimeters has never been reported and
15 formulated before. Using the discrete element method, we then develop a
16 comprehensive saltation model, in which the triboelectric charging between particle-
17 particle midair collisions is explicitly accounted for, allowing us to evaluate the
18 triboelectric charging in saltation properly. By combining the results of measurements
19 and modelling, we find that although the vertical component of the E-field (i.e. 1-D E-
20 field) inhibits sand transport, 3-D E-field enhances sand transport substantially.
21 [Furthermore, the model predicts that 3-D E-field enhances the total mass flux and](#)
22 [saltation height by up to 20 % and 15 %, respectively.](#) This suggests that a truly 3-D E-
23 field consideration is necessary if one is to explain precisely how the E-field affects
24 saltation during dust storms. These results will further improve our understanding of
25 particle triboelectric charging in saltation and help to provide more accurate
26 characterizations of sand and dust transport during dust storms.

27

28 **1. Introduction**

29 Contact or triboelectric charging is a ubiquitous phenomenon in dust events

1 (Harrison et al., 2016; Kok and Renno, 2008; Lacks and Sankaran, 2011; Schmidt et al.,
2 1998; Zheng et al., 2003). The pioneering electric field (E-field) measurements in dust
3 storms by W. A. Douglas Rudge showed that the vertical atmospheric E-field was
4 substantially increased to 5-10 kV m⁻¹ and reversed its direction (became upward-
5 pointing) during a severe dust storm (Rudge, 1913). Later measurements in dust
6 storms found downward-pointing (Esposito et al., 2016), upward-pointing (Bo and
7 Zheng, 2013; Yair et al., 2016; Zhang and Zheng, 2018), and even alternating vertical
8 E-field which continually reverses direction (Kamra, 1972; Williams et al., 2009), with
9 the magnitude of up to ~100 kV m⁻¹.

10 The significant influences of E-field on the lifting and transport of sand and dust
11 particles have been verified, both numerically (e.g. Kok and Renno, 2008; Zhang et al.,
12 2014) and experimentally (e.g. Esposito et al., 2016; Rasmussen et al., 2009). The
13 effects of E-field on saltation, however, remain obscure. A clear discrepancy between
14 numerical simulation and field measurement is that: numerical simulation showed a
15 reduction in saltation mass flux by E-field (e.g. Kok and Renno, 2008; Zheng et al., 2003),
16 whereas recent field measurements found a dramatic increase in dust concentration
17 (up to a factor of 10) by E-field (Esposito et al., 2016), suggesting that E-field might
18 enhance saltation mass flux. This is probably because most previous numerical
19 simulations only considered the vertical component of the E-field (i.e. 1-D), but there
20 also in fact exist streamwise and spanwise components of E-field in dust events. For
21 example, Jackson and Farrell (2006) recorded the horizontal component of the E-field
22 of up to 120 kV m⁻¹ in dust devils. Zhang and Zheng (2018) also found the streamwise
23 and spanwise components (termed horizontal component) of the E-field of up to 150
24 kV m⁻¹ in dust storms. Hence, E-field is actually three-dimensional (3-D). In many cases,
25 the magnitude of the horizontal component is larger than that of the vertical
26 component. The horizontal component should therefore not be neglected when
27 evaluating the role of E-field in saltation during dust storms.

28 Most field observations, such as Schmidt et al. (1998) and Bo et al. (2014), studied
29 the electrical properties of sand particles in dust events. However, these studies are

1 generally not conclusive because the charge transfer between contacting particles are
2 sensitive to ambient conditions. For example, Schmidt et al. (1998) found that the
3 mean charge-to-mass ratio of saltating particles at 5 cm height was $+60 \mu\text{C kg}^{-1}$, which
4 did not agree with their finding of upward-pointing vertical E-field. This
5 inconclusiveness may be attributed to environmental (lurking) factors, such as relative
6 humidity, soil moisture, surface crust, etc., are not fully controllable (recorded) in the
7 field observations. The uncertainties in field observations provide motivation for
8 numerical studies of the particle triboelectric charging in saltation. In addition, unlike
9 pure saltation (that is, no suspended dust particles), the dust storm is a very complex
10 dusty phenomenon that is made up by numerous polydisperse particles embedded in
11 a high Reynolds-number turbulent flow. Such high complexity of dust storms
12 challenges the accurate simulation of 3-D E-field in dust storms. It is therefore more
13 straightforward to characterize 3-D E-field experimentally.

14 In this study, we evaluate the effects of 3-D E-field on saltation during dust storms
15 by combining measurements and modelling. To reveal the properties of 3-D E-field, we
16 simultaneously measured the 3-D E-fields in the sub-meter layer from 0.05 to 0.7 m
17 above the ground during a dust storm. Such vertical profile of the 3-D E-field in the
18 sub-meter layer has not been previously characterized. To reveal how 3-D E-field
19 affects saltation, we develop a comprehensive numerical model of particle
20 triboelectric charging in saltation. In this model, the charge transfers between
21 contacting particles are explicitly calculated, but the 3-D E-field is formulated directly
22 based on the data measured in our measurements, due to its huge challenges in
23 modelling. The effects of various important parameters, such as the density of charged
24 species and the [height-averaged time-varying mean of the 3-D E-field](#), are also
25 investigated and described herein.

26

27 **2. Field campaign**

28 **2.1 Observational set-up and uncertainty**

29 We performed 3-D E-field measurements at the Qingtu Lake Observation Array

1 (QLOA) site (approximately $39^{\circ}12'27''$ N, $103^{\circ}40'03''$ E, as shown in Fig. 1a), in
2 May 2014. The measured physical quantities include: wind velocities at four heights
3 measured by the sonic anemometers (CSAT3B, Campbell Scientific, Inc.) with 50 Hz
4 sampling frequency; number of saltating particle passing through the measurement
5 area ($2\text{ mm}\times 25\text{ mm}$) per second at 6 heights measured by sand particle counter (SPC-
6 91, Niigata Electric Co., Ltd.) with 1 Hz sampling frequency, thus providing an
7 estimation of the size distribution of saltating particles, saltation mass flux, and
8 saltation height (Text S1 in the Supplement); 3-D E-field at five heights measured by
9 the vibrating-reed E-field mill (VREFM, developed by Lanzhou University) with 1 Hz
10 sampling frequency. The layout of all instruments is shown in Fig. 1b. All instruments
11 are powered by solar panels. The detailed descriptions of the QLOA site and VREFM
12 sensor can be found in our previous studies (e.g. Zhang et al., 2017; Zheng, 2013).

13 The measurement uncertainties in our field campaign are threefold: wind velocity
14 (CSAT3B), particle mass flux (SPC-91), and E-field (VREFM). The CSAT3B is factory
15 calibrated with an accuracy of $\pm 8\text{ cm s}^{-1}$. The SPC-91 is factory calibrated by a set of
16 filamentation wires of equivalent diameters from 0.138 to 0.451 mm, with an
17 uncertainty of $\pm 0.015\text{ mm}$. The VREFM used in the field measurements is carefully
18 calibrated and selected in our lab by a parallel-plate E-field calibrator (Zhang et al.,
19 2017), and its maximum uncertainties range from $\sim 1.38\%$ to $\sim 2.24\%$ (see Text S2 in
20 the Supplement).

22 **2.2 Data analysis**

23 In general, the actual wind direction exits a specific angle from the prevailing wind
24 direction. A projection step is therefore needed to obtain the streamwise E-field, E_1 ,
25 and spanwise E-field, E_2 . For example, E_1 is equal to the sum of the projection of the
26 measured E_x and E_y (E-field in the direction of x and y axes, as shown in Fig. 1b)
27 to the streamwise wind direction.

28 After completing the projection step, we then perform the following steps
29 sequentially to reveal the pattern of 3-D E-field in the sub-meter layer: (1) estimating

1 time-varying mean values of E-field; (2) computing height-averaged time-varying mean
2 in the measurement region from 0.05 to 0.7 m above the ground; (3) normalizing E-
3 field by height-averaged mean values; and (4) finally fitting the vertical profiles of
4 normalized E-field by the 3-order polynomial functions. It is worth noting that the
5 measured time series in dust storms are generally non-stationary when viewed as a
6 whole (e.g. Zhang and Zheng, 2018). In such cases, the statistical values are time-
7 varying. Here, we use the discrete wavelet transform (DWT) method (Daubechies,
8 1990) and the ensemble empirical mode decomposition (EEMD) method (Wu and
9 Huang, 2009), which are widely used in various geophysical studies (e.g. Grinsted et
10 al., 2004; Huang and Wu, 2008; Wu et al., 2011), to estimate the time-varying mean
11 values of the measured non-stationary 3-D E-field data. We select these two methods
12 since the DWT with higher orders of Daubechies wavelet (e.g. db10) and the EEMD can
13 extract a reasonable and physically meaningful time-varying mean (Su et al., 2015).
14 Each step for revealing the 3-D E-field pattern is described in detail as follows:

15 The DWT uses a set of mutually orthogonal wavelet basis functions, which are
16 dilated, translated and scaled versions of a mother wavelet, to decompose an E-field
17 series $E(t, z)$ into a series of successive octave band components (Percival and
18 Walden, 2000), i.e.,

19

$$20 \quad E(t, z) = \sum_{i=1}^N \psi_i(t, z) + \chi_N(t, z) \quad (1)$$

21

22 Where N is the total number of decomposition levels, $\psi_i(t, z)$ denotes the i -th
23 level wavelet detail component, and $\chi_N(t, z)$ represents the N -th level wavelet
24 approximation (or smooth) component. As N increases, the frequency contents
25 become lower and thus the N -th level approximation component could be regarded
26 as the time-varying mean values (e.g. Percival and Walden, 2000; Su et al., 2015). In
27 this study, the DWT decomposition is performed with the Daubechies wavelet of order
28 10 (db10) at level 10, and thus the 10-th order approximation component can be

1 defined as the time-varying mean:

2

$$3 \quad \bar{E}(t, z) = \chi_{10}(t, z) \quad (2)$$

4

5 which reflect the averages of the $E(t, z)$ series over a scale of 2^{10} s (about 17.1
6 minutes).

7 On the other hand, according to the empirical mode decomposition (EMD)
8 method, the time series $E(t, z)$ can be decomposed as (Huang et al., 1998)

9

$$10 \quad E(t, z) = \sum_{i=1}^N \xi_i(t, z) + \eta_N(t, z) \quad (3)$$

11

12 through a sifting process, where $\xi_i(t, z)$ ($i = 1, 2, \dots, N$) are the intrinsic mode
13 functions (IMFs), and $\eta_N(t, z)$ is a residual (which is the overall trend or mean). To
14 reduce the end effects and mode mixing in EMD, the EEMD method is proposed by Wu
15 and Huang (2009). In EEMD, a set of white noise series, $w_j(t, z)$ ($j = 1, 2, \dots, N_e$), are
16 added to the original signal $E(t, z)$. Then, each noise-added series is decomposed into
17 IMFs followed by the same sifting process as in EMD. Finally, the i -th EEMD
18 component is defined as the ensemble mean of the i -th IMFs of the total of N_e
19 noise-added series (see Wu and Huang, 2009 for details).

20 In this study, the time-varying mean values $\bar{E}(t, z)$ can be alternatively defined
21 as the sum of the last four EEMD components, $\xi_{10}(t, z)$ to $\xi_{13}(t, z)$, and the residual,
22 $\eta_{13}(t, z)$, i.e.

23

$$24 \quad \bar{E}(t, z) = \sum_{i=10}^{13} \xi_i(t, z) + \eta_{13}(t, z) \quad (4)$$

25

26 which is approximately the 17.3 minutes (very close to the timescale of ~ 17.1 minutes
27 used in DWT) or longer timescale variability trend (Wu et al., 2011), because the

1 maximum mean frequency of the last four EEMD components is 5.78×10^{-2} Hz (see Figs.
2 S5 and S6 in the Supplement for details).

3 According to the above definitions, the time-varying mean can be obtained by the
4 DWT and EEMD methods over the timescale of about 17 minutes. As an example, Fig.
5 2 shows the results of db10 DWT analysis (Fig. 2b) and EEMD decompositions (Fig. 2c)
6 for an E-field time series $E(t, z)$ in our field campaign. It can be seen that DWT and
7 EEMD can properly capture the time-varying mean over the timescale of 17 minutes,
8 with very little difference between the two methods.

9 Since the 3-D E-field are measured at five heights in our field campaign, we thus
10 define the height-averaged time-varying mean values as

11

$$12 \quad \langle \overline{E}_i(t, z) \rangle = \left| \frac{1}{(0.7 - 0.05)} \int_{0.05}^{0.7} \overline{E}_i(t, z) dz \right| \quad (5)$$

13

14 in the range of 0.05 to 0.7 m height, in order to normalize the E-field data by a unified
15 quantity. Further, the E-field data can be normalized as

16

$$17 \quad E_i^+(t, z) = \frac{E_i(t, z)}{\langle \overline{E}_i(t, z) \rangle} \quad (6)$$

18

19 Additionally, to obtain the dimensionless vertical profile of 3-D E-field, the height z
20 should also be a dimensionless parameter. Here, the dimensionless height z^+ is
21 defined as the ratio of height z to the mean saltation height \bar{z}_{salt} during the whole
22 observed dust storm, i.e.

23

$$24 \quad z^+ = \frac{z}{\bar{z}_{salt}} \quad (7)$$

25

26 where the saltation height z_{salt} during a certain time interval is defined as the height
27 below which 99 % of the total mass flux is present and can be estimated based on the

1 measured SPC-91 data (see Text S1 in the Supplement for details).

2 Finally, the dimensionless vertical profiles of 3-D E-field at different periods are
3 **together** fitted by the 3-order polynomial functions:

$$4 \quad E_i^+(z^+) = a_{0,i} + a_{1,i}z^+ + a_{2,i}(z^+)^2 + a_{3,i}(z^+)^3, \quad i = 1,2,3 \quad (8)$$

6
7 where $i = 1, 2,$ and 3 correspond to the streamwise, spanwise, and vertical
8 components, respectively.

9 10 **3. Saltation model**

11 For modelling steady-state saltation, there are four primary processes, including
12 (1) particle saltating motion, (2) particle-particle midair collisions, (3) particle-bed
13 collisions, and (4) particle-wind momentum coupling (Dupont et al., 2013; Kok and
14 Renno, 2009). Also, the changes in both momentum and electrical charge of each
15 particle are taken into account in the particle-particle midair and particle-bed collisions.
16 To avoid overestimating midair collisions in 2-D simulation (Carneiro et al., 2013), we
17 simulate saltation trajectories in a real 3-D domain. We use the discrete element
18 method (DEM), which explicitly simulates each particle motion and describes the
19 collisional forces between colliding particles encompassing normal and tangential
20 components, to advance the evaluation of the effects of particle midair collisions. In
21 the following subsections, we will describe each process in detail.

22 23 **3.1 Size distribution of particle sample**

24 Granular materials in natural phenomena, such as sand, aerosols, pulverized
25 material, seeds of crops, etc., are made up of discrete particles with a wide range of
26 sizes ranging from a few micrometers to millimeters. The log-normal distribution is
27 generally used to approximate the size distribution of the sand sample (Dupont et al.,
28 2013; Marticorena and Bergametti, 1995). Thus, the mass distribution function of a
29 sand sample with two parameters, average diameter d_m , and geometric standard

1 deviation σ_p , can be written as

2

$$3 \quad \frac{dM(d_p)}{d\ln(d_p)} = \frac{1}{\sqrt{2\pi}\ln(\sigma_p)} \exp\left\{-\frac{[\ln(d_p) - \ln(d_m)]^2}{2[\ln(\sigma_p)]^2}\right\} \quad (9)$$

4

5 **3.2 Equations of saltating particles motion**

6 The total force acting on a saltating particle consists of three distinct interactions
 7 (Minier, 2016). The first one refers to the wind-particle interaction, which is dominated
 8 by the drag force with lifting forces such as Saffman force and Magnus force being of
 9 secondary importance (Dupont et al., 2013; Kok and Renno, 2009). The second
 10 interaction refers to the particle-particle collisional forces or cohesion caused by
 11 physical contact between particles. Such interparticle collisional forces can be
 12 described as a function of the overlaps between the colliding particles. The third
 13 interaction refers to the forces due to external fields such as gravity and E-field. In this
 14 study, in addition to the drag force, we also take into account the Magnus force
 15 because of the remarkable rotation of saltating particles on the order of 100-1000 rev
 16 s⁻¹ (Xie et al., 2007). The effects of electrostatic forces on particle motion, which are
 17 significant for large wind velocity (Schmidt et al., 1998; Zheng et al., 2003), are also
 18 taken into account. Consequently, the full governing equations of saltating particles
 19 can be written as

20

$$21 \quad m_{p,i} \frac{d\vec{u}_{p,i}}{dt} = \vec{F}_i^d + \vec{F}_i^m + \sum_j (\vec{F}_{ij}^n + \vec{F}_{ij}^t) + m_i \vec{g} + \zeta_{p,i} \vec{E} \quad (10a)$$

$$22 \quad I_i \frac{d\vec{\omega}_{p,i}}{dt} = \vec{M}_i^{w-p} + \sum_j (\vec{M}_{ij}^c + \vec{M}_{ij}^r) \quad (10b)$$

23

24 where $m_{p,i}$ is the mass of the i -th particle; $\vec{u}_{p,i}$ is the velocity of the particle; \vec{F}_i^d is
 25 the drag force; \vec{F}_i^m is the Magnus force; \vec{F}_{ij}^n and \vec{F}_{ij}^t are the normal and tangential
 26 collisional forces from the j -th particle, respectively; \vec{g} is the gravitational

1 acceleration; $\zeta_{p,i}$ is the charge-to-mass ratio of the sand particles and will be altered
 2 during every collision (see section 3.4); \vec{E} is the 3-D E-field given by our
 3 measurements; I_i is the moment of inertia; $\vec{\omega}_{p,i}$ is the angular velocity of the
 4 particle; \vec{M}_i^{w-p} is the torque caused by the wind on the particle; \vec{M}_{ij}^c and \vec{M}_{ij}^r are
 5 the tangential torque due to the tangential component of the particle collisional forces
 6 and the rolling resistance torque, respectively. The summation Σ represents
 7 considering all particles that are in contact with the i -th particle.

8

9 **3.2.1 Wind-particle interactions**

10 In the absence of saltating particles, the mean wind profile over a flat and
 11 homogeneous surface is well approximated by the log-law (Anderson and Haff, 1988)

12

$$13 \quad u_m(z) = \frac{u_*}{\kappa} \ln \frac{z}{z_0} \quad (11)$$

14

15 where u_m is the mean streamwise wind speed; z is the height above the surface;
 16 u_* is the friction velocity; $\kappa \approx 0.41$ is the von Kármán constant; z_0 is the
 17 aerodynamic roughness, which varies substantially from different flow conditions and
 18 can be approximately estimated as $d_m/30$ for the aeolian saltation on Earth (e.g.
 19 Carneiro et al., 2013; Kok et al., 2012). In the presence of saltation, due to the
 20 momentum coupling between the saltating particles and wind flow, the modified wind
 21 speed gradient can be written as (e.g. Kok and Renno, 2009; Pähtz et al., 2015)

22

$$23 \quad \frac{du_m(z)}{dz} = \frac{u_*}{\kappa z} \sqrt{1 - \frac{\tau_p(z)}{\rho_a u_*^2}} \quad (12)$$

24

25 where ρ_a is the air density, $\tau_p(z)$ is the particle momentum flux and can be
 26 numerically determined by (Carneiro et al., 2013; Shao, 2008)

27

$$\tau_p(z) = -\frac{\sum m_{p,i} u_{p,i} w_{p,i}}{L_x L_y \Delta z} \quad (13)$$

with L_x , L_y , and Δz being the streamwise-, spanwise-width of the computational domain, and vertical grid size, respectively; $u_{p,i}$ and $w_{p,i}$ are the streamwise and vertical components of particle velocity. The summation in Eq. (13) is performed on the particles located in the range of $[z, z + \Delta z]$. Once saltating particle trajectories are known, the wind profile can be determined through integrating Eq. (12) with the no-slip boundary condition $u_m = 0$ at $z = z_0$.

Since sand particles are much heavier than the air and are well smaller than the Kolmogorov scales, the drag force is the dominant force affecting particle motion, which is expressed by (Anderson and Haff, 1991)

$$\vec{F}_i^d = -\frac{\pi d_p^2}{8} \rho_a C_d \vec{u}_r |\vec{u}_r| \quad (14)$$

where d_p is the diameter of the particle; C_d is the drag coefficient; and $\vec{u}_r = \vec{u}_p - \vec{u}_w$ is the particle-to-wind relative velocity. The drag coefficient C_d is a function of the particle Reynolds number, $Re_p = \rho_a |\vec{u}_r| d_p / \mu$, where μ is the dynamic viscosity of the air. We calculate the drag coefficient by an empirical relation $C_d = \left[(32/Re_p)^{2/3} + 1 \right]^{3/2}$, which is applicable to the regimes from Stokes flow $Re_p \ll 1$ to high Reynolds number turbulent flow (Cheng, 1997).

Additionally, we also account for the effects of particle rotation on particle motion using the Magnus force expressed as (Anderson and Hallet, 1986; Loth, 2008; White and Schulz, 1977)

$$\vec{F}_i^m = \frac{\pi d_p^2}{8} \rho_a C_m (\vec{\omega}_{p,i} \times \vec{u}_r) \quad (15)$$

where C_m is a normalized spin lift coefficient depended on the particle Reynolds

1 number and the circumferential speed of the particle. The torque acting on a particle
 2 caused by wind flow is calculated from (Anderson and Hallet, 1986; Kok and Renno,
 3 2009; Shao, 2008)

$$4 \quad \vec{M}_i^{w-p} = \pi \mu d_i^3 \left(\frac{1}{2} \frac{du_m}{dz} - \vec{\omega}_i \right) \quad (16)$$

7 3.2.2 Particle-particle midair collisions

8 Under moderate conditions, saltation is a dilute flow in which the particle-particle
 9 collisions are negligible. However, as wind velocity increases, midair collisions become
 10 increasingly pronounced, especially in the near-surface region. For spherical particles,
 11 one of the most commonly-used collisional force model is the nonlinear viscoelastic
 12 model, consisting of two components, i.e. elastic and viscous forces (Brilliantov et al.,
 13 1996; Haff and Anderson, 1993; Silbert et al., 2001; Tulev et al., 2010).

14 Considering two spherical particles i and j with diameters d_i and d_j , and
 15 position vectors \vec{x}_i and \vec{x}_j , are in contact with each other. The relative velocity \vec{v}_{ij}
 16 at the contact point and its normal and tangential components, \vec{v}_{ij}^n and \vec{v}_{ij}^t , are
 17 respectively defined as (Norouzi et al., 2016; Silbert et al., 2001)

$$18 \quad \vec{v}_{ij} = \vec{u}_{p,i} - \vec{u}_{p,j} + 0.5(d_i \vec{\omega}_{p,i} + d_j \vec{\omega}_{p,j}) \times \vec{n}_{ij} \quad (17a)$$

$$19 \quad \vec{v}_{ij}^n = (\vec{v}_{ij} \cdot \vec{n}_{ij}) \vec{n}_{ij} \quad (17b)$$

$$20 \quad \vec{v}_{ij}^t = \vec{v}_{ij} - \vec{v}_{ij}^n \quad (17c)$$

21
 22
 23 where $\vec{n}_{ij} = (\vec{x}_j - \vec{x}_i) / |\vec{x}_j - \vec{x}_i|$ is the unit vector in the direction from the center
 24 of particle i point toward the center of particle j . Suppose that these colliding
 25 particles having identical mechanical properties with Young's modulus Y , shear
 26 modulus G , and Poisson's ratio ν , and thus the normal collisional force can be
 27 calculated by (Brilliantov et al., 1996; Silbert et al., 2001)

1

2

$$\vec{F}_{ij}^n = -\frac{4}{3}Y^*\sqrt{R^*}\delta_n^{3/2}\vec{n}_{ij} - 2\sqrt{\frac{5}{6}m^*S_n\beta v_n}\vec{n}_{ij} \quad (18)$$

3

4

5

6

7

8

9

10

11

12

13

14

$$\vec{F}_{ij}^t = \begin{cases} -8G^*\sqrt{R^*}\delta_n\delta_t\vec{t}_{ij} - 2\sqrt{\frac{5}{6}m^*S_t\beta v_t}\vec{t}_{ij}, & \text{if } |\vec{F}_{ij}^t| \leq \gamma_s|\vec{F}_{ij}^n| \\ -\gamma_s|\vec{F}_{ij}^n|\vec{t}_{ij}, & \text{if } |\vec{F}_{ij}^t| > \gamma_s|\vec{F}_{ij}^n| \end{cases} \quad (19)$$

15

16

17

18

19

20

21

22

23

24

$$\vec{M}_{ij}^c = 0.5d_i\vec{n}_{ij} \times \vec{F}_{ij}^t \quad (20)$$

To account for the significant rolling friction, we apply a rolling resistance torque

1 (Ai et al., 2011)

2

$$3 \quad \vec{M}_{ij}^r = -\gamma_r R^* |\vec{F}_{ij}^n| \vec{\omega}_{ij} \quad (21)$$

4

5 on each colliding particle, where μ_r is the coefficient of rolling friction, and $\vec{\omega}_{ij} =$
6 $(\vec{\omega}_{p,i} - \vec{\omega}_{p,j}) / |\vec{\omega}_{p,i} - \vec{\omega}_{p,j}|$ is the unit vector of relative angular velocity.

7

8 **3.3 Particle-bed collisions**

9 As a saltating particle collides with the sand bed, it has not only a chance to
10 rebound but also may eject several particles from the sand bed. For simplicity, we use
11 a probabilistic representation, termed as “splash function”, to describe the particle-
12 bed interactions quantitatively (Kok et al., 2012; Shao, 2008). Currently, the splash
13 function is primarily characterized by wind-tunnel and numerical simulations (e.g.
14 Anderson and Haff, 1991; Haff and Anderson, 1993; Huang et al., 2017; Rice et al.,
15 1996). The rebounding probability of a saltating particle colliding with the sand bed is
16 approximately by (Anderson and Haff, 1991)

17

$$18 \quad P_{reb} = 0.95[1 - \exp(-v_{imp})] \quad (22)$$

19

20 where v_{imp} is the impact speed of the saltating particle. The kinetic energy of the
21 rebounding particles is taken as 0.45 ± 0.22 of the impact particle (Kok and Renno,
22 2009). The rebounding angles θ and φ , as depicted in Fig. 3a, obey an exponential
23 distribution with a mean value of 40° , i.e. $\theta \sim \text{Exp}(40^\circ)$, and a normal distribution
24 with parameters $0 \pm 10^\circ$, i.e. $\varphi \sim \text{N}(0^\circ, 10^\circ)$, respectively (Dupont et al., 2013; Kok
25 and Renno, 2009).

26 It is reasonable to assume that the number of ejected particles depends on the
27 impact speed and its cross-sectional area. Thus, the number of ejected particles from
28 the k -th particle bin is (Kok and Renno, 2009)

1

2

$$N_k = \frac{0.02}{\sqrt{gD_{250}}} \frac{D_{imp}}{D_{eje}^k} p_k v_{imp} \quad (23)$$

3

4

5

6

7

8

9

10

11

3.4 Particle charge exchanges

12

13

14

15

16

17

18

$$\Delta q_{ij} = -e(\rho_h^j S_j - \rho_h^i S_i) \quad (24)$$

19

20

21

22

23

24

25

26

where $e = 1.602 \times 10^{-19}$ C is the elementary charge; ρ_h^i is the density of the electrons trapped in the high energy states on the surface of particle i (assuming that all particles have an identical initial value ρ_h^0), which is modified as $\rho_{h,i}^{\text{after}} = \rho_{h,i}^{\text{before}} + (\rho_h^j S_j - \rho_h^i S_i) / (\pi d_i^2)$ due to collisions between particle i and j ; S_i is the particle contact area, which can be approximately calculated as a line integral along the contact path L_i of particle i

$$S_i = 2 \int_{L_i} \sqrt{R^* \delta_n} dl_i \quad (25)$$

2

3 where dl_i is the differential of the contact length. In general, when two particles are
 4 in contact with each other, the relative sliding motion between the two particles
 5 results in two unequal contact areas S_i and S_j , thus producing net charge transfer
 6 Δq_{ij} between the two particles. If the particle's net electrical charge is known, its
 7 charge-to-mass ratio can be easily determined.

8

9 **3.5 Particle-phase statistics**

10 Similar to particle momentum flux (i.e. Eq. 13), particle horizontal mass flux q ,
 11 total mass flux Q , mean particle mass concentration m_c , and mean particle
 12 horizontal speed $\langle u_p \rangle$ can be numerically determined by (Carneiro et al., 2013;
 13 Dupont et al., 2013)

14

$$q(z) = \frac{\sum m_{p,i} u_{p,i}}{L_x L_y \Delta z} \quad (26a)$$

$$Q = \frac{\sum m_{p,i} u_{p,i}}{L_x L_y} \quad (26b)$$

$$m_c(z) = \frac{\sum m_{p,i}}{L_x L_y \Delta z} \quad (26c)$$

$$\langle u_p \rangle(z) = \frac{\sum u_{p,i}}{L_x L_y \Delta z} \quad (26d)$$

19

20 where the summation \sum is performed over the saltating particles located in the range
 21 of $[z, z + \Delta z]$ for q , m_c , and $\langle u_p \rangle$, but it is performed over all saltating particles for
 22 Q .

23

24 **3.6 Model implementation**

1 We consider polydisperse soft-spherical sand particles having log-normal mass
2 distribution in a 3-D computational domain 0.5 m×0.1 m×1.0 m (as shown in Fig. 3a),
3 with periodic boundary condition in the x and y directions. Here, the upper
4 boundary is set to be high enough so that the particle escapes from the upper
5 boundary can be avoided. To reduce the computational cost, the spanwise dimension
6 is chosen as $L_y = 0.1$, since the saltating particles are mainly moving along the
7 streamwise direction.

8 As shown in Fig. 3b, the model is initiated by randomly releasing 100 uncharged
9 particles, within the region below 0.3 m, and then such released particles begin to
10 move under the action of the initial log-law wind flow, triggering saltation through a
11 series of particle-bed collisions. We use cell-based collision searching algorithms,
12 which perform collision search for particles located in the target cell and its
13 neighboring cells, to find the midair colliding pairs. The random processes, particle-
14 bed collisions described previously, are simulated using a general method called the
15 inverse transformation. The particle motion and wind flow equations are integrated by
16 predictor-corrector method AB3AM4; that is, 3-order Adams-Bashforth method to
17 perform prediction and 4-order Adams-Moulton method to perform the correction.
18 One of the main advantages of using such multi-step integration method is that the
19 accuracy of results is not sensitive to the detection of exact moments of collision (Tuley
20 et al., 2010). The charge transfer between the colliding pairs is caused by their
21 asymmetric contact and can be determined by Eqs. (24) and (25). When calculating
22 particle-bed charge transfer, the bed is regarded as an infinite plane. According to the
23 law of charge conservation, the surface charge density of the infinite bed plane and
24 the newly ejected particles, σ , is (Kok and Renno, 2008; Zhang et al., 2014)

$$\sigma = - \int_{z_0}^{+\infty} \rho_c(z) dz \quad (27)$$

27
28 where ρ_c is the space charge density. For modelling pure saltation, the E-field is

1 calculated by Gauss's law (e.g. Zhang et al., 2014). For modelling saltation during dust
2 storms, the 3-D E-field is directly formulated by Eq. (8) based on our field
3 measurements, as mentioned above. The variables used in this study are listed and
4 described in Table 1.

5

6 **4. Results**

7 **4.1. Vertical profiles of 3-D E-field**

8 On May 6, 2014, field measurements began at ~12:00 due to the limited power
9 supply by solar panels. As shown in Fig. 4, although the early stage of dust storm has
10 not been observed, we successfully recorded data of about 8 hours, which is
11 substantial enough to reveal the pattern of 3-D E-field. From Fig. 4, it can be seen that,
12 in general, the streamwise and spanwise components (up to ~80 kV m⁻¹) are
13 consistently larger than the vertical component of the E-field (up to ~40 kV m⁻¹). The
14 vertical profiles of the normalized streamwise, spanwise, and vertical components of
15 E-field are shown in Figs. 5a-5c, respectively. Note that there is little difference
16 between the DWT and EEMD results, because these are the mean values over the
17 ~17.1 and ~17.3 minutes timescales, respectively. To the best of our knowledge, these
18 data are the first measured 3-D E-field data in the sub-meter layer during dust storms.
19 Numerous studies showed that the vertical component of E-field in pure saltation
20 decreased with increasing height (e.g., Kok and Renno, 2008; Schmidt et al., 1998;
21 Zhang et al., 2014). Interestingly, Fig. 5c shows that during dust storms, all normalized
22 components, E_1^+ to E_3^+ , decreases monotonically as height increases in the saltation
23 layer (i.e. $z^+ \leq 1$), similar to the pattern of vertical component in pure saltation.

24 As shown in Figs. 5a-5c, in different periods, each component of the normalized
25 3-D E-field roughly collapses on a single 3-order polynomial curve (with $R^2=0.67-0.97$,
26 see Table 2 for details). This suggests that during dust storms, the 3-D E-field in the
27 sub-meter layer can be characterized as $\langle \overline{E}_i \rangle E_i^+$, where E_i^+ represents the pattern
28 of the dimensionless E-field vertical profile (formulated by Eq. 8), and $\langle \overline{E}_i \rangle$ represents
29 the height-averaged time-varying mean defined in Eq. (5). It is worth noting that the

1 E-field pattern E_i^+ and their intensities $\langle \overline{E_i} \rangle$ are strongly depended on the saltation
2 conditions, such as dust mass loading, temperature, relative humidity (RH), etc. For
3 example, at given ambient temperature and RH, the mean E-field intensities $\langle \overline{E_i} \rangle$
4 increases linearly with dust mass loading (e.g. Esposito et al., 2016; Zhang et al., 2017).
5 In addition, both E_i^+ and $\langle \overline{E_i} \rangle$ could vary from event to event, among them, the
6 saltation conditions are quite different. So far, a quantitative representation of $\langle \overline{E_i} \rangle$ is
7 challenging due to its high complexity, and thus we regard it as a basic parameter in
8 the following sections for exploring the effects of 3-D E-field on saltation. The fitting
9 results of Eq. (8) are listed in Table 2, with coefficients as rounded to two decimals. The
10 formulations of the 3-D E-field can be readily substituted into the numerical model (i.e.
11 Eq. 10a).

13 **4.2. Effects of particle-particle midair collisions on saltation**

14 Before quantifying the effects of 3-D E-field on saltation by our numerical model,
15 we draw a comparison of several key physical quantities between the simulated results
16 and measurements in the case of pure saltation, in order to ensure the convergence
17 and validity of our numerical code, as shown in Figs. 6a-6c. It is clearly shown that the
18 saltation eventually reaches a dynamic steady-state after ~ 4 seconds. The number of
19 the impacting particles (~ 72 grains) is equal to the sum of the rebounding (~ 50 grains)
20 and the ejected particles (~ 22 grains) during the time interval of 10^{-4} s. At steady-state,
21 each impacting particle, on average, produces a single saltating particle, either by
22 rebound or by ejection. As shown in Fig. 6b, the total mass flux is well predicted by our
23 numerical model, and midair collisions enhance the total mass flux dramatically,
24 especially for less particle viscous dissipation (i.e. large e_n) and large friction velocity.
25 Also, the predicted charge-to-mass ratios of saltating particles are widely distributed
26 from -400 to $+60 \mu\text{C kg}^{-1}$, consistent with the previous measurements of charge-to-
27 mass ratio in pure saltation (Bo et al., 2014; Schmidt et al., 1998; Zheng et al., 2003).
28 In addition to affecting sand transport, midair collisions also affect charge exchanges

1 between saltating particles. When considering midair collisions, the charge-to-mass
2 ratio distribution shifts slightly toward zero as the wind velocity increases, as shown in
3 Figs. 7a-7c.

4 5 **4.3. Effects of 3-D E-field on saltation**

6 By substituting the formulations of the 3-D E-field (i.e. $\langle \overline{E}_i \rangle E_i^+$, $i = 1,2,3$) into
7 our model (i.e. Eq. 10a), we then evaluate the effects of 3-D E-field on saltation during
8 storms properly. As shown in Fig. 8a, compared to the case without E-field, the vertical
9 component of the E-field (i.e. 1-D E-field) inhibits mass flux, in agreement with
10 previous studies (Kok and Renno, 2008; Zheng et al., 2003). However, the mass flux is
11 enhanced by 3-D E-field, causing the simulated value closer to our measured data.
12 Such enhancement of mass flux by 3-D E-field can be qualitatively explained by the
13 considerable enhancements of m_c below ~ 0.02 m height (Fig. 9a) and $\langle u_p \rangle$ in the
14 range from 0.01 to 0.1 m height (Fig. 9b), due to the streamwise and spanwise
15 components. Meanwhile, although the saltation height is not sensitive to E-field
16 vertical component, 3-D E-field enhances the saltation height significantly and,
17 therefore, makes the numerical prediction more accurate (Fig. 8b). This is because
18 when considering the E-field vertical component, the mass flux profile is very similar
19 to the case of no E-field consideration (Figs. 8a and 9). In contrast, 3-D E-field causes a
20 distortion of the mass flux profile (as well as m_c and $\langle u_p \rangle$), and thus alters saltation
21 height significantly (Figs. 8a and 9).

22 Additionally, we also explore how the key parameter, density of charged species
23 ρ_h^0 , affects saltation, as shown in Figs. 10a-10c. Since the height-averaged time-varying
24 mean is strongly depended on the ambient conditions such as temperature and RH,
25 the height-averaged time-varying mean is set at two different levels. The predicted
26 results show that, at each height-averaged time-varying mean level, the magnitude of
27 the charge-to-mass ratio increases with increasing ρ_h^0 , and then reaches a relatively
28 equilibrium value at approximately $\rho_h^0 = 10^{16}$ m⁻² (Fig. 10a), thus leading to a
29 constant enhancement of total mass flux Q and saltation height z_{salt} (Figs. 10b and

1 10c). For the larger height-averaged time-varying mean, the enhancements of the total
2 mass flux Q and saltation height z_{salt} could exceed 20 % and 15 %, respectively.

3 4 **5. Discussion**

5 **5.1. Field measurements of 3-D E-field in the sub-meter layer**

6 To determine the effects of particle triboelectric charging on saltation precisely,
7 3-D E-field measurements in the saltation layer (i.e. sub-meter above the ground) is
8 required. Although the E-field measurements, such as Bo and Zheng (2013), Esposito
9 et al. (2016), Kamra (1972), Rudge (1913), Williams et al. (2009), and Zhang et al. (2017)
10 in dust storms are numerous, 3-D E-field in the sub-meter layer have not been studied
11 so far. This is because the traditional atmospheric E-field sensors, such as CS110 sensor
12 manufactured by Campbell Scientific, Inc., have dimensions of $15.2 \times 15.2 \times 43.2 \text{ cm}^3$
13 (e.g. Esposito et al., 2016; Yair et al., 2016), which is too large compared to the height
14 of saltation layer. Thus, it will lead to significant disturbances of the ambient E-field.
15 Fortunately, the diameter of the VREFM sensor developed by Lanzhou University is
16 only 2 cm and thus could considerably eliminate the E-field disturbances (Zhang et al.,
17 2017; Zheng, 2013). In this study, using the VREFM sensors, we have measured and
18 characterized the 3-D E-field from 0.05 to 0.7 m height during dust storms, which can
19 provide valuable data for investigating the mechanisms of particle triboelectric
20 charging in saltation.

21 In E-field data analysis, the E-field is normalized by its time-varying mean over the
22 timescale of approximately 17 minutes, which can be extracted by the DWT and EEMD
23 methods with negligible end effects and mode mixing (Percival and Walden, 2000; Wu
24 and Huang, 2009). At the same time, since the saltation height z_{salt} slightly varies
25 with time (i.e. $0.172 \pm 0.0343 \text{ m}$, see Fig. S3 in the supplement), the height z above
26 the ground is normalized by the mean saltation height \bar{z}_{salt} . Note that we calculate
27 the saltation height and mass flux over every 30-min time interval because the
28 sufficiently long period is needed to capture all scales of turbulence (Martin and Kok,
29 2017; Sherman and Li, 2012). The 3-D E-field pattern is finally characterized as the 3-

1 order polynomials, but it is only valid in the range that is not too far beyond the
2 measurement points. Additionally, the 3-D E-field pattern of dust storms may vary
3 event to event, because it is strongly related to the driving mechanisms of dust storms,
4 such as monsoon winds, squall lines, and thunderstorms (Shao, 2008), and ambient
5 conditions, such as temperature and relative humidity (Esposito et al., 2016; Zhang
6 and Zheng, 2018). Although the 3-D E-field pattern revealed in this study may not be
7 a universal feature, the proposed E-field data analysis method can be easily applied to
8 other cases.

10 **5.2. An entirely distinct 3-D E-field in the saltation layer during dust storms**

11 Like many previous studies, the E-field can be simplified to 1-D (i.e. vertical
12 component) in pure saltation (e.g. Kok and Renno, 2008), since in such cases the
13 magnitude of the streamwise and spanwise components is much less than that of
14 vertical component (Zhang et al., 2014). However, during dust storms, the streamwise
15 and spanwise components are consistently larger than the vertical component, as
16 mentioned previously. E-field is therefore 3-D. In contrast to the vertical component,
17 which is closely related to the total mass loading (Esposito et al., 2016; Williams et al.,
18 2009), the intense streamwise and spanwise components are aerodynamically created
19 due to the nonuniform transport of charged particles in the [streamwise and spanwise](#)
20 [directions](#) (Zhang et al., 2014). It is well-known that dust storm is a polydisperse
21 [particle-laden turbulent flow at very high-Reynolds-number \(up to \$\sim 10^8\$ \)](#). During dust
22 [storms, the particle transport is regulated by the large- and very-large-scale motions](#)
23 [of wind flows \(Jacob and Anderson, 2016\)](#), which may lead to the phenomenon that
24 [the charged particles are more nonuniformly distributed \(over a larger spatial scale\) in](#)
25 [dust storms than in pure saltation](#).

27 **5.3. Particle-particle triboelectric charging resolved model**

28 Although most physical mechanisms, such as asymmetric contact, polarization by
29 external E-fields, statistical variations of material properties and shift of aqueous ions,

1 are responsible for particle triboelectric charging, contact or triboelectric charging is
2 the primary mechanism (e.g. Harrison et al., 2016; Lacks and Sankaran, 2011; Zheng,
3 2013). In previous model, however, the charge-to-mass ratios of the saltating particles
4 are either assumed to be a constant value (e.g. Schmidt et al., 1998; Zhang et al., 2014;
5 Zheng et al., 2003), or are not accounted for in the particle-particle midair collisions
6 (e.g. Kok and Renno, 2008). In this study, by using DEM together with an asymmetric
7 contact electrification model, we account for the particle-particle triboelectric
8 charging during midair collisions in saltation. [The DEM implemented by cell-based](#)
9 [algorithms is effectively to detect and evaluate most of the particle-particle midair](#)
10 [collisional dynamics \(Norouzi et al., 2016\)](#). Meanwhile, the charge transfer between
11 colliding particles can be determined by Eqs. (24) and (25). Compared to the previous
12 studies (e.g. Kok and Lacks, 2009), the main innovation of this model is that the
13 comprehensive consideration of the particle collisional dynamics affecting particle
14 charge transfer is involved. In summary, the present model is a particle-particle midair
15 collision resolved model, and the predicted charge-to-mass ratio agrees well with the
16 published measurement data (see Fig. 6c). These findings indicate that midair
17 collisions in saltation are important, both in momentum and charge exchanges.

19 **5.4. Implications for evaluating particle triboelectric charging in dust events**

20 It is generally accepted that E-field could considerably affect the lifting and
21 transport of sand particles. As the findings of previous 1-D E-field models (e.g. Kok and
22 Renno, 2008), the E-field has been proven to inhibit sand transport in our model, when
23 considering the vertical component of the E-field alone. In contrast to the 1-D E-field,
24 our model further shows that the real 3-D E-field in dust storms enhances sand
25 transport substantially, consistent with a recent measurement by Esposito et al. (2016).
26 [This 3-D E-field model may resolve the discrepancy between the 1-D E-field model \(e.g.](#)
27 [Kok and Renno, 2008\) and the recent measurement \(i.e. Esposito et al., 2016\)](#). In
28 [addition, the saltation height has also been enhanced by 3-D E-field](#). Therefore, it is
29 [necessary to consider 3-D E-field in further studies](#).

1 However, a remaining critical challenge is still to simulate particle triboelectric
2 charging in dust storms precisely. The driving atmospheric turbulent flows having a
3 typical Reynolds number on the order of 10^8 cover a broad range of length and time
4 scales, which needs huge computational cost to resolve (e.g. Shao, 2008). On the other
5 hand, particle triboelectric charging is so sensitive to particle's collisional dynamics
6 that it needs to resolve each particle collisional dynamics (e.g. Hu et al., 2012; Lacks
7 and Sankaran, 2011). To model the particle's collisional dynamics properly, the time
8 steps of DEM are generally from 10^{-7} to 10^{-4} s (Norouzi et al., 2016). However, steady-
9 state saltation motion often requires several seconds to several tens of seconds to
10 reach the equilibrium state. In this study, when $u_* = 0.5 \text{ m s}^{-1}$ and the computational
11 domain is $0.5 \times 0.1 \times 1.0 \text{ m}^3$, the total number of saltating particles exceeds 7×10^4 (Fig.
12 S8 in the Supplement). Consequently, the triboelectric charging in saltation is currently
13 very difficult to simulate, where a large number of polydisperse sand particles, the high
14 Reynolds-number turbulent flow, and the inter-particle electrostatic forces are
15 mutually coupled. In the present version of the model, we do not consider the particle-
16 particle interactions such as particle agglomeration and fragmentation during particle
17 collision or frictional contact, as well as the particle-turbulence interaction that is the
18 effects of turbulent fluctuations on the triboelectric charging and dynamics of particles.
19 Further studies require considerable effort to incorporate these interactions,
20 especially turbulence, which is very important for large wind velocity.

21 22 **6. Conclusions**

23 Severe dust storms occurring in arid and semiarid regions threaten human lives
24 and result in substantial economic damages. Intense E-field up to $\sim 100 \text{ kV m}^{-1}$ does
25 exist in dust storms and could strongly affect particle dynamics. In this study, we
26 performed the field measurements of 3-D E-field in the sub-meter layer from 0.05 to
27 0.7 m above the ground during dust storms by VREFM sensors. Meanwhile, by
28 introducing the DEM and asymmetric charging mechanism into the saltation model,
29 we numerically study the effects of 3-D E-field on saltation. Overall, our results show

1 that: (1) measured 3-D E-field data roughly collapse on the 3-order polynomial curves
2 when normalized, providing a simple representation of the 3-D E-field during dust
3 storms for the first time; (2) the inclusion of 3-D E-field in saltation model may resolve
4 the discrepancy between previous 1-D E-field model (e.g. Kok and Renno, 2008) and
5 measurements (Esposito et al., 2016) in the aspect of whether the E-field inhibits or
6 enhances saltation; (3) midair collisions dramatically affect both momentum and
7 charge exchanges between saltating particles; and (4) the model predicts that 3-D E-
8 field enhances the total mass flux and saltation height significantly, suggesting that 3-
9 D E-field should be considered in future models, especially for dust storms.

10 We have also performed discussions about various sensitive parameters such as
11 the density of charged species, the coefficient of restitution, and the height-averaged
12 time-varying mean of the 3-D E-field. These results significantly add new knowledge to
13 the role of particle triboelectric charging in determining the transport and lifting of
14 sand and dust particles. A great effort is further needed to understanding the
15 interactions such as particle agglomeration and fragmentation, as well as the effects
16 of the turbulence on the triboelectric charging and dynamics of particles.

17

18 **Data availability**

19 The E-field data recorded in our field campaign are provided as a CSV file in the
20 Supplement.

21

22 **Author contribution**

23 H.Z. performed the field observations, numerical simulation, and data analyses as
24 well as wrote the manuscript, which was guided and edited by Y.H.Z. All authors
25 discussed the results and commented on the manuscript.

26

27 **Competing interests**

28 The authors declare that they have no conflict of interest.

29

1 **Acknowledgments**

2 We thank the editor, Markku Kulmala, and two anonymous reviewers for their
3 comprehensive and insightful comments that greatly improve the final manuscript.

4 This work was supported by the National Natural Science Foundation of China (grant
5 numbers 11802109 and 11490553), the Young Elite Scientists Sponsorship Program by
6 CAST (grant number 2017QNR001), and the Fundamental Research Funds for the
7 Central Universities (grant number lzujbky-2018-7).

9 **References**

10 Ai, J., Chen, J. F., Rotter, J. M., and Ooi, J. Y.: Assessment of rolling resistance models in
11 discrete element simulations, *Powder Technol.*, 206, 269–282,
12 doi:10.1016/j.powtec.2010.09.030, 2011.

13 Anderson, R. S., and Hallet, B.: Sediment transport by wind: toward a general model,
14 *Geol. Soc. Am. Bull.*, 97, 523-535, doi: 10.1130/0016-
15 7606(1986)97<523:STBWTA>2.0.CO;2, 1986.

16 Anderson, R. S., and Haff, P. K.: Simulation of eolian saltation, *Science*, 241, 820–823,
17 doi:10.1126/science.241.4867.820, 1988.

18 Anderson, R. S., and Haff, P. K.: Wind modification and bed response during saltation
19 of sand in air, *Acta Mech.*, 1, 21–51, doi:10.1007/978-3-7091-6706-9_2, 1991.

20 Bagnold, R.: *The Physics of Blown Sand and Desert Dunes*, Chapman & Hall, London,
21 1941.

22 Bo, T. L., Zhang, H., and Zheng, X. J.: Charge-to-mass ratio of saltating particles in wind-
23 blown sand, *Sci. Rep.*, 4, 5590, doi:10.1038/srep05590, 2014.

24 Bo, T. L., and Zheng, X. J.: A field observational study of electrification with in a dust
25 storm in Minqin, China, *Aeolian Res.*, 8, 39–47, doi:10.1016/j.aeolia.2012.11.001,
26 2013.

27 Brilliantov, N. V., Spahn, F., Hertzsch, J. M., and Poschel, T.: Model for collisions in
28 granular gases, *Phys. Rev. E*, 53, 5382, doi:10.1103/PhysRevE.53.5382, 1996.

29 Carneiro, M. V., Araújo, N. A., Pähtz, T., and Herrmann, H. J.: Midair collisions enhance

1 saltation, *Phys. Rev. Lett.*, 115, 058001, doi:10.1103/PhysRevLett.111.058001,
2 2013.

3 Cheng, N. S.: Simplified settling velocity formula for sediment particle, *J. Hydraul. Eng.*,
4 123, 149–152, doi:10.1061/(ASCE)0733-9429(1997)123:2(149), 1997.

5 Dupont, S., Bergametti, G., Marticorena, B., and Simoens, S.: Modeling saltation
6 intermittency, *J. Geophys. Res.-Atmos.*, 118, 7109–7128, doi:10.1002/jgrd.50528,
7 2013.

8 Esposito, F., Molinaro, R., Popa, C.I., Molfese, C., Cozzolino, F., Marty, L., Taj-Eddine, K.,
9 Achille, G. D., Franzese, G., and Silvestro, S.: The role of the atmospheric electric
10 field in the dust lifting process, *Geophys. Res. Lett.*, 43, 5501–5508,
11 doi:10.1002/2016GL068463, 2016.

12 [Grinsted, A., Moore, J. C., and Jevrejeva, S.: Application of the cross wavelet transform
13 and wavelet coherence to geophysical time series, *Nonlinear Proc. Geoph.*, 11,
14 561-566, doi: 10.5194/npg-11-561-2004, 2004.](#)

15 Haff, P. K., and Anderson, R. S.: Grainscale simulations of loose sedimentary beds: the
16 example of grain-bed impacts in aeolian saltation, *Sedimentology*, 40, 175–198,
17 doi:10.1111/j.1365-3091.1993.tb01760.x, 1993.

18 Harrison, R. G., Barth, E., Esposito, F., Merrison, J., Montmessin, F., Aplin, K. L., Borlina,
19 C., Berthelier, J. J., Dprez, G., and Farrell, W. M.: Applications of electrified dust
20 and dust devil electrostatics to martian atmospheric electricity, *Space Sci. Rev.*,
21 203, 299–345, doi:10.1007/s11214-016-0241-8, 2016.

22 Hu, W., Xie, L., and Zheng, X.: Contact charging of silica glass particles in a single
23 collision, *Appl. Phys. Lett.*, 101, 114107, doi:10.1063/1.4752458, 2012.

24 [Huang, H. J., Bo, T. L., and Zhang, R.: Exploration of splash function and lateral velocity
25 based on three-dimensional mixed-size grain/bed collision. *Granul. Matter*, 19\(4\),
26 73, doi: 10.1007/s10035-017-0759-9, 2017.](#)

27 Huang, N. E., Shen, Z., Long, S. R., Wu, M. C., Shih, H. H., Zheng, Q., Yen, N. C., Tung, C.
28 C., and Liu, H. H.: The empirical mode decomposition and the Hilbert spectrum
29 for nonlinear and non-stationary time series analysis, *Proc. R. Soc. A-Math. Phys.*

1 Eng. Sci., 454, 903–995, doi:10.1098/rspa.1998.0193, 1998.

2 Huang, N. E., and Wu, Z.: A review on Hilbert-Huang transform: Method and its
3 applications to geophysical studies, *Rev. Geophys.*, 46, RG2006,
4 doi:10.1029/2007RG000228, 2008.

5 Jackson, T. L., and Farrell, W. M.: Electrostatic fields in dust devils: an analog to Mars,
6 *IEEE Trans. Geosci. Remote Sensing*, 44, 2942–2949,
7 doi:10.1109/TGRS.2006.875785, 2006.

8 Kamra, A. K.: Measurements of the electrical properties of dust storms, *J. Geophys.*
9 *Res.*, 77, 5856–5869, doi:10.1029/JC077i030p05856, 1972.

10 Kawamura, R.: Study on sand movement by wind, Technical Report, Institute of Science
11 and Technology, University of Tokyo, 5, 95–112, 1951.

12 Kok, J. F., and Lacks, D. J.: Electrification of granular systems of identical insulators, *Phys.*
13 *Rev. E*, 79, 051304, doi:10.1103/PhysRevE.79.051304, 2009.

14 Kok, J. F., Parteli, E. J., Michaels, T. I., and Karam, D. B.: The physics of wind-blown sand
15 and dust, *Rep. Prog. Phys.*, 75, 106901, doi:10.1088/0034-4885/75/10/106901,
16 2012.

17 Kok, J. F., and Renno, N. O.: Electrostatics in wind-blown sand, *Phys. Rev. Lett.*, 100,
18 014501, doi:10.1103/PhysRevLett.100.014501, 2008.

19 Kok, J. F., and Renno, N. O.: A comprehensive numerical model of steady state saltation
20 (COMSALT), *J. Geophys. Res.-Atmos.*, 114, doi:10.1029/2009JD011702, 2009.

21 Lacks, D. J., and Sankaran, R. M.: Contact electrification of insulating materials, *J. Phys.*
22 *D-Appl. Phys.*, 44, 453001, doi:10.1088/0022-3727/44/45/453001, 2011.

23 Lettau, K., and Lettau, H. H.: Experimental and micro-meteorological field studies of
24 dune migration, in Lettau, K., and Lettau, H. H., eds., *Exploring the World's Driest*
25 *Climate*, Institute for Environmental Studies, University of Wisconsin Madison,
26 110–147, 1978.

27 Loth, E.: Lift of a spherical particle subject to vorticity and/or spin, *AIAA J.*, 46, 801–
28 809, doi:10.2514/1.29159, 2008.

29 Marticorena, B., and Bergametti, G.: Modeling the atmospheric dust cycle: 1. design

1 of a soil-derived dust emission scheme, *J. Geophys. Res.-Atmos.*, 100, 16415–
2 16430, doi:10.1029/95JD00690, 1995.

3 [Martin, R. L., and Kok, J. F.: Wind-invariant saltation heights imply linear scaling of
4 aeolian saltation flux with shear stress, *Sci. adv.*, 3, doi: 10.1126/sciadv.1602569,
5 2017.](#)

6 Minier, J. P.: Statistical descriptions of polydisperse turbulent two-phase flows, *Phys.*
7 *Rep.*, 665, 1–122, doi:10.1016/j.physrep.2016.10.007, 2016.

8 Norouzi, H. R., Zarghami, R., Sotudeh-Gharebagh, R., and Mostoufi, N.: Coupled CFD-
9 DEM modeling: formulation, implementation and application to multiphase flows,
10 John Wiley & Sons, Chichester, 2016.

11 Owen, P. R.: Saltation of uniform grains in air, *J. Fluid Mech.*, 20, 225–242,
12 doi:10.1017/S0022112064001173, 1964.

13 Pähtz, T., Omeradžić, A., Carneiro, M. V., Araújo, N. A., and Herrmann, H. J.: Discrete
14 Element Method simulations of the saturation of aeolian sand transport, *Geophys.*
15 *Res. Lett.*, 42, 2063–2070, doi:10.1002/2014GL062945, 2015.

16 [Percival, D. B., Walden, A. T.: *Wavelet methods for time series analysis*, Cambridge, UK,
17 Cambridge UP, 2000.](#)

18 Rasmussen, K. R., Kok, J. F., and Merrison, J. P.: Enhancement in wind-driven sand
19 transport by electric fields, *Planet Space Sci.*, 57, 804–808,
20 doi:10.1016/j.pss.2009.03.001, 2009.

21 Rice, M. A., Willetts, B. B., and McEwan, I. K.: Observations of collisions of saltating
22 grains with a granular bed from high-speed cine-film, *Sedimentology*, 43, 21-31,
23 doi:10.1111/j.1365-3091.1996.tb01456.x, 1996.

24 Rudge, W. A. D.: Atmospheric electrification during South African dust storms, *Nature*,
25 91, 31–32, doi:10.1038/091031a0, 1913.

26 Schmidt, D. S., Schmidt, R. A., and Dent, J. D.: Electrostatic force on saltating sand, *J.*
27 *Geophys. Res.-Atmos.*, 103, 8997–9001, doi:10.1029/98JD00278, 1998.

28 Shao, Y. P.: *Physics and Modelling of Wind Erosion*, Springer Science & Business Media,
29 Heidelberg, 2008.

- 1 Sherman, D. J., and Li, B.: Predicting aeolian sand transport rates: A reevaluation of
2 models, *Aeolian Res.*, 3, 371-378, doi: 10.1016/j.aeolia.2011.06.002, 2012.
- 3 Silbert, L. E., Ertaş, D., Grest, G. S., Halsey, T. C., Levine, D., and Plimpton, S. J.: Granular
4 flow down an inclined plane: Bagnold scaling and rheology, *Phys. Rev. E*, 64,
5 051302, doi:10.1103/PhysRevE.64.051302, 2001.
- 6 Sørensen, M.: On the rate of aeolian transport, *Geomorphology*, 59, 53–62,
7 doi:10.1016/j.geomorph.2003.09.005, 2004.
- 8 Su, Y., Huang, G., and Xu, Y. L.: Derivation of time-varying mean for non-stationary
9 downburst winds, *J. Wind Eng. Ind. Aerod.*, 141, 39-48, doi:
10 10.1016/j.jweia.2015.02.008, 2015.
- 11 Tuley, R., Danby, M., Shrimpton, J., and Palmer, M.: On the optimal numerical time
12 integration for lagrangian dem within implicit flow solvers, *Comput. Chem. Eng.*,
13 34, 886–899, doi:10.1016/j.compchemeng.2009.10.003, 2010.
- 14 White, B. R., and Schulz, J. C.: Magnus effect in saltation, *J. Fluid Mech.*, 81, 497–512,
15 doi:10.1017/S0022112077002183, 1977.
- 16 Williams, E., Nathou, N., Hicks, E., Pontikis, C., Russell, B., Miller, M., and Bartholomew,
17 M. J.: The electrification of dust-lofting gust fronts (haboobs) in the sahel, *Atmos.*
18 *Res.*, 91, 292–298, doi:10.1016/j.atmosres.2008.05.017, 2009.
- 19 Wu, Z., and Huang, N. E.: Ensemble empirical mode decomposition: a noise-assisted
20 data analysis method, *Adv. Adaptive Data Anal.*, 1, 1-41, doi:
21 10.1142/S1793536909000047, 2009.
- 22 Wu, Z., Huang, N. E., Wallace, J. M., Smoliak, B. V., and Chen, X.: On the time-varying
23 trend in global-mean surface temperature, *Clim. Dyn.*, 37, 759–773,
24 doi:10.1007/s00382-011-1128-8, 2011.
- 25 Xie, L., Ling, Y., and Zheng, X.: Laboratory measurement of saltating sand particles’
26 angular velocities and simulation of its effect on saltation trajectory, *J. Geophys.*
27 *Res.-Atmos.*, 112, D12116, doi:10.1029/2006JD008254, 2007.
- 28 Yair, Y., Katz, S., Yaniv, R., Ziv, B., and Price, C.: An electrified dust storm over the Negev
29 desert, *Israel, Atmos. Res.*, 181, 63–71, doi:10.1016/j.atmosres.2016.06.011,

1 2016.

2 Zhang, H., Bo, T. L., and Zheng, X.: Evaluation of the electrical properties of dust storms
3 by multi-parameter observations and theoretical calculations, *Earth Planet. Sci.*
4 *Lett.*, 461, 141–150, doi:10.1016/j.epsl.2017.01.001, 2017.

5 Zhang, H., and Zheng, X.: Quantifying the large-scale electrification equilibrium effects
6 in dust storms using field observations at Qingtu Lake Observatory, *Atmos. Chem.*
7 *Phys.*, 18, 17087–17097, doi:10.5194/acp-18-17087-2018, 2018.

8 Zhang, H., Zheng, X. J., and Bo, T. L.: Electrification of saltating particles in wind-blown
9 sand: Experiment and theory, *J. Geophys. Res.-Atmos.*, 118, 12,086-12,093.
10 doi:10.1002/532 2013JD020239, 2013.

11 Zhang, H., Zheng, X. J., and Bo, T. L.: Electric fields in unsteady wind-blown sand, *Eur.*
12 *Phys. J. E*, 37, 13, doi:10.1140/epje/i2014-14013-6, 2014.

13 Zheng, X. J.: Electrification of wind-blown sand: recent advances and key issues, *Eur.*
14 *Phys. J. E*, 36, 138, doi:10.1140/epje/i2013-13138-4, 2013.

15 Zheng, X. J., Huang, N., and Zhou, Y. H.: Laboratory measurement of electrification of
16 wind-blown sands and simulation of its effect on sand saltation movement, *J.*
17 *Geophys. Res.-Atmos.*, 108, doi:10.1029/2002JD002572, 2003.

18

1 **Table 1.** Description of all variables used in this study.

Symbols	Physical meaning	Units
$a_{0,i}, a_{1,i}, a_{2,i}, a_{3,i}$	fitting coefficients in Eq. (8)	1
C_d	drag coefficient	1
C_m	normalized spin lift coefficient in Magnus force formula	1
d_p	particle diameter	m
d_i, d_j	diameters of particle i and j	m
d_m	mean diameter of particle sample in the numerical model	m
D_{imp}, D_{ej}^k	diameter of the impact and ejected particles	m
e_n	coefficient of restitution of particles	1
$E(t, z)$	a time series of measured E-field	kV m ⁻¹
$\bar{E}(t, z)$	time-varying mean values of $E(t)$	kV m ⁻¹
$\langle \bar{E}_i(t, z) \rangle$	height-averaged time-varying mean values of $E(t)$	kV m ⁻¹
$E_i^+(z^+)$	dimensionless E-field of component i	1
E_1, E_2, E_3	streamwise, spanwise, and vertical components of E-field	kV m ⁻¹
\vec{F}_i^d, \vec{F}_i^m	drag force and Magnus force acting on particle i	N
$\vec{F}_{ij}^d, \vec{F}_{ij}^t$	the normal and tangential collisional forces	N
$g=9.81$	gravitational acceleration	m s ⁻²
G	shear modulus of particles	Pa
G^*	equivalent shear modulus between two contacting particles	Pa
I_i	moment of inertia of particle i	kg m ²
L_x, L_y	streamwise and spanwise width of the computational domain	m
m^*	equivalent particle mass between two contacting particles	kg
$m_{p,i}$	mass of particle i	kg
m_c	mean particle mass concentration	kg m ⁻³
$\vec{M}_i^{w-p}, \vec{M}_{ij}^c, \vec{M}_{ij}^r$	torque due to the wind, the torque due to the tangential component of the particle collisional forces, and the rolling resistance torque	N·m
\vec{n}_{ij}	unit vector in the direction from the center of particle i point toward the center of particle j	-
N	number of the decomposition levels of DWT and EEMD	1
N_e	number of white noise series added to the original E-field series	1
N_k	number of ejected particles from the k -th particle bin	1
p_k	mass fraction of the k -th particle bin	1
P_{reb}	rebouncing probability of a saltating particle colliding with the sand bed	1
q, Q	mass flux and total mass flux defined in Eq. (26)	kg m ⁻² s ⁻¹ , Kg m ⁻¹ s ⁻¹
R^*	equivalent particle radius between two contacting particles	m
Re_p	particle Reynolds number	1
S_i, S_j	contact area of particle i and j	m ²
\vec{u}_r	particle-to-wind relative velocity	m s ⁻¹
u_m	mean streamwise wind speed	m s ⁻¹
u_*	friction velocity	m s ⁻¹

Table 1. Continued.

Symbols	Physical meaning	Units
$\vec{u}_{p,i}$	velocity of particle i	m s^{-1}
$u_{p,i}, w_{p,i}$	streamwise and vertical components of particle velocity	m s^{-1}
$\langle u_p \rangle$	mean particle horizontal speed	m s^{-1}
v_{imp}	impact speed of the saltating particle	m s^{-1}
$\vec{v}_{ij}, \vec{v}_{ij}^n, \vec{v}_{ij}^t$	relative velocity between particle i and j at the contact point, and its normal and tangential components	m s^{-1}
\vec{x}_i, \vec{x}_j	position vectors of particle i and j	m
$Y=10^8$	Young's modulus of particles	Pa
Y^*	equivalent Young's modulus between two contacting particles	Pa
z, z^+	height above the ground and dimensionless height	$\text{m}, 1$
z_0	the aerodynamic roughness	m
z_{salt}	saltation height	m
β	damping coefficient of collisional forces	1
$\gamma_s=0.5, \gamma_r=0.1$	coefficients of static and rolling friction	1
$\zeta_{p,i}$	charge-to-mass ratio of particle i	C kg^{-1}
η_n	residual of EEMD or EMD	-
θ, φ	rebouncing angles of particles	$^\circ$
$\kappa \approx 0.41$	von Kármán constant	1
τ_p	particle momentum flux	Pa
$\vec{\omega}_{p,i}$	angular velocity of the particle i	rad s^{-1}
δ_n, δ_t	normal and tangential overlap between two contacting particles	m
$\mu=1.8 \times 10^{-5}$	dynamic viscosity of the air	$\text{Pa}\cdot\text{s}$
$\nu=0.3$	Poisson's ratio of particles	1
ξ_i	EEMD component or IMF of EMD	-
$\rho_a=1.174$	air density	kg m^{-3}
$\rho_p=2650$	particle mass density	kg m^{-3}
ρ_c	space charge density	C m^{-3}
ρ_h^i, ρ_h^j	density of the electrons trapped in the high energy states on the surface of particle i and j	m^{-2}
σ	surface charge density	C m^{-2}
σ_p	geometric standard deviation of particle sample in the numerical model	1
$\chi_N(t, z)$	the i -th level wavelet detail component	-
$\psi_i(t, z)$	the N -th level wavelet approximation component	-
Δq_{ij}	net increment of the charge of particle i after colliding with particle j	C
Δz	vertical grid size	m

1

2

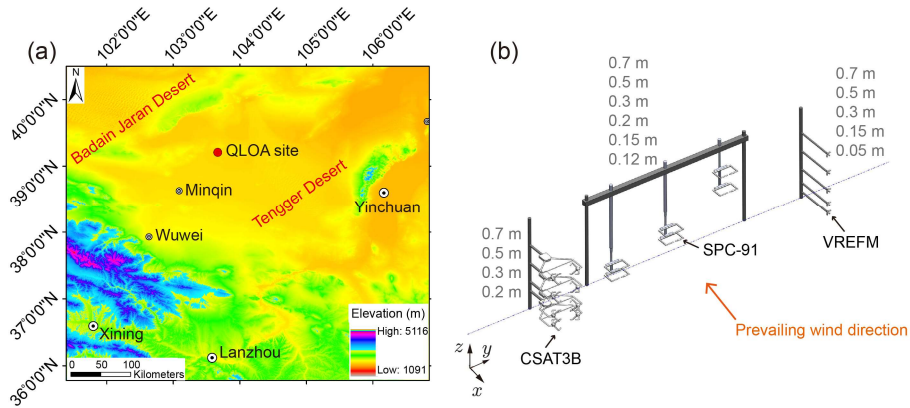
1 **Table 2.** Fitting coefficients of the 3-order polynomial curves in Fig. 5.

Components	$a_{0,i}$	$a_{1,i}$	$a_{2,i}$	$a_{3,i}$	R^2
$i = 1$	-2.17	4.02	-2.24	0.31	0.97
$i = 2$	-0.71	2.06	-1.49	0.23	0.80
$i = 3$	0.55	-1.41	1.24	-0.21	0.67

2

3

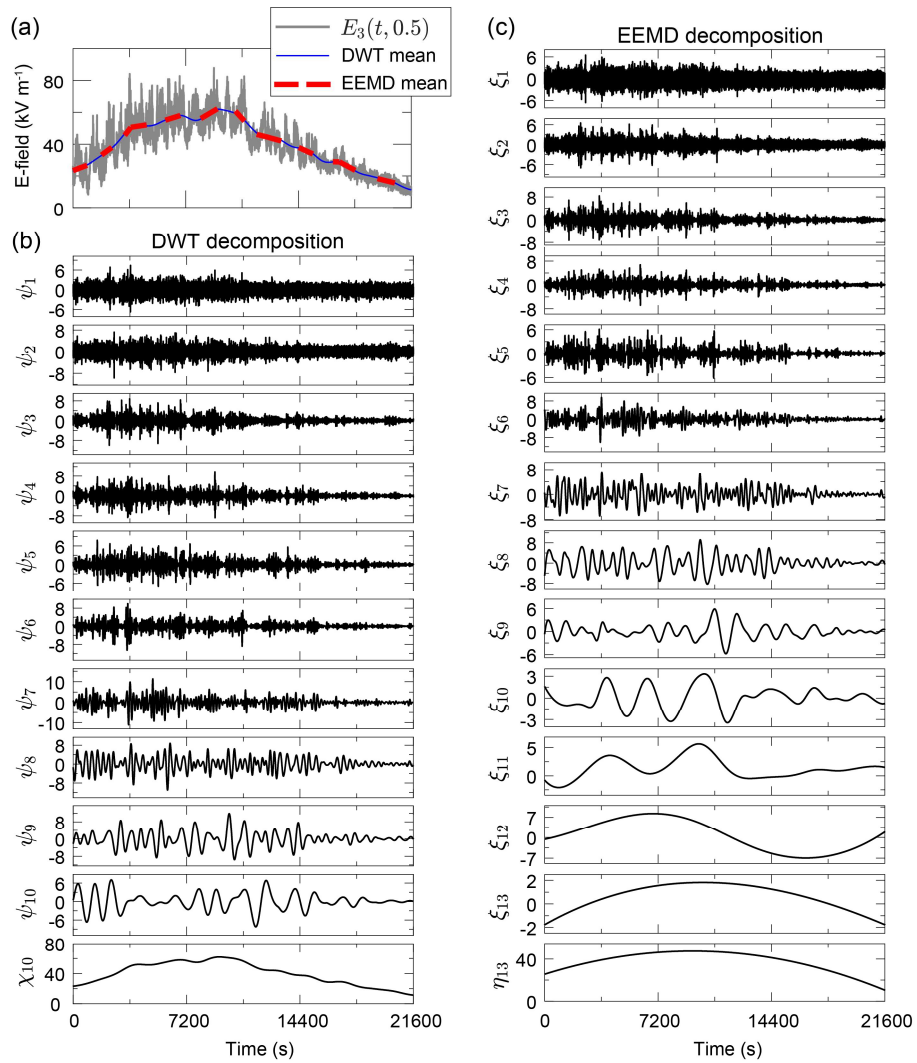
1



2

3 **Figure 1.** Map of the QLOA site and the layout of all instruments. (a) The QLOA site is
4 located between the Badain Jaran Desert and the Tengger Desert, approximately 90
5 km northeast of Minqin, Gansu, China. (b) Four CSAT3B sensors were mounted at 0.2-
6 0.7 m height, respectively; six SPC-91 sensors were mounted at 0.12-0.7 m height,
7 respectively; total fifteen VREFM sensors were mounted to measure the 3-D E-field at
8 0.05-0.7 m height, respectively (that is, at each measurement point, three VREFM
9 sensors are mutually perpendicular). The CSAT3B, SPC-91, and VREFM sensors were
10 distributed along a straight line parallel to the y axis, and the prevailing wind
11 direction in the QLOA site is parallel to the x axis.

12



2

3 **Figure 2.** The resulting DWT and EEMD components from a measured vertical E-field4 component at 0.5 m height, $E_3(t, 0.5)$, with a total of $N_d=21600$ data points. (a)

5 shows the original E-field time series (gray line), and the time-varying mean obtained

6 by DWT (red line) and EEMD (blue dashed line). (b) shows the detailed components

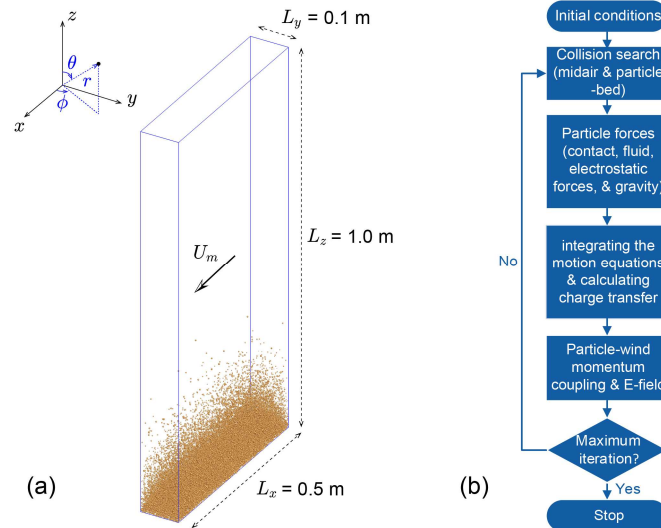
7 $\psi_1 - \psi_{10}$ and approximation component χ_{10} of DWT. (c) shows the EEMD8 components $\xi_1 - \xi_{13}$ and the residue η_{13} . In the EEMD, N is specified as $\log_2(N_d) -$ 9 1, the member of ensemble N_e is 100, and the added white noise in each ensemble

10 member has a standard deviation of 0.2. Times are shown relative to May 6, 2014 at

11 13:00:00 UTC+8.

12

1

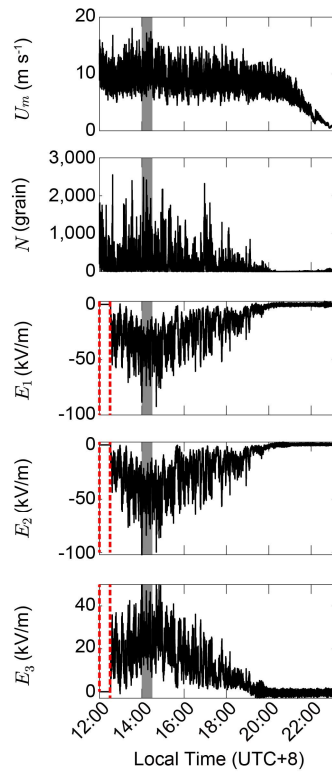


2

3 **Figure 3.** A schematic illustration of the DEM simulation of saltation and the numerical
4 algorithm of the saltation model. (a) A 3-D view of the simulated wind-blown sand at
5 the steady state, where the wind shear velocity $u_* = 0.5 \text{ m s}^{-1}$, average sand diameter
6 $d_m = 228 \text{ }\mu\text{m}$, and geometric standard deviation $\sigma_p = \exp(0.3)$. Both the Cartesian and
7 spherical coordinates are shown in the inset. (b) This flowchart shows the scheme for
8 simulating the saltation according to the following steps implementing the DEM with
9 particle triboelectric charging: initial conditions, collision search, particle forces,
10 integrating motion equations and calculating charge transfer, particle-wind
11 momentum coupling and evaluating E-field, and finally repeating these execute steps
12 until reaching the maximum iteration steps.

13

1

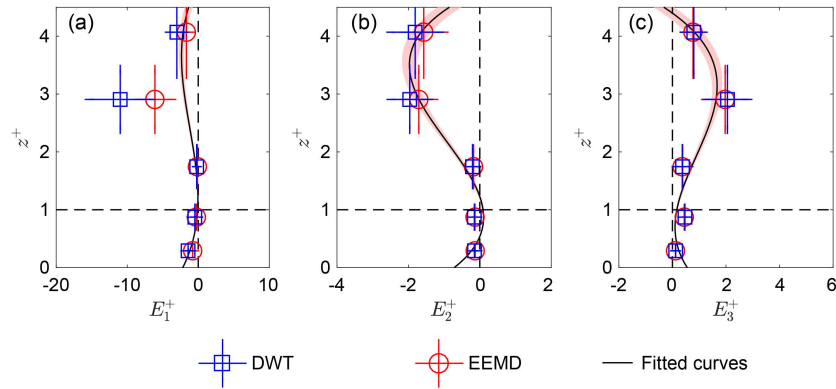


2

3 **Figure 4.** Measured results during a dust storm occurring on May 6, 2014, at the QLOA
4 site. (a)-(e): the measured time series of the streamwise wind speed, u_m at 0.7 m;
5 the number of saltating particle N at 0.15 m; streamwise E-field E_1 , spanwise E-field
6 E_2 , and vertical E-field E_3 at 0.7 m. Unfortunately, owing to the interruption of power
7 supply, the 3-D E-field data have not been recorded before $\sim 12:30$, as represented by
8 a dashed box in the last three panels (from top to bottom). The shaded area denotes
9 the relatively stationary period of the observed dust storm.

10

1



2

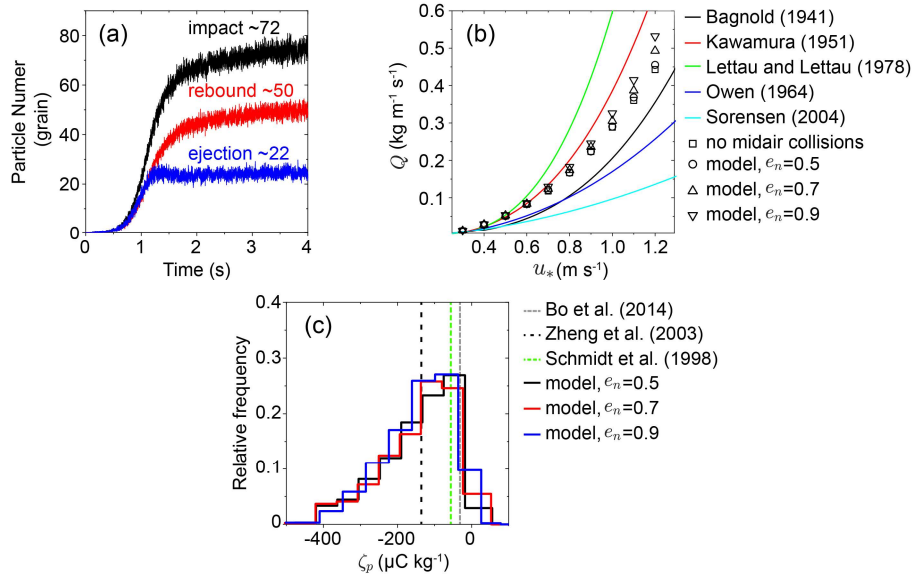
3 **Figure 5.** Vertical profiles of the normalized 3-D E-field. Subgraphs (a)-(c), in turn,
4 correspond to the vertical profiles of E_1^+ , E_2^+ , and E_3^+ of the observed dust storm.

5 Squares and circles denote the DWT mean and EEMD mean values of the normalized
6 E-field data, respectively. Error bars are standard deviations. Lines denote robust linear

7 least-squares fitting of the normalized E-field data obtained by DWT and EEMD
8 method using 3-order polynomials (with R^2 of 0.97, 0.80, and 0.67, respectively),

9 where the shaded areas denote 95% confidence bounds.

10



2

3 **Figure 6.** Verification of the steady-state numerical model in the case of pure saltation.

4 That is, only vertical E-field needs to be considered, which is produced by the charged

5 saltating particles. (a) The number of the impacting, rebounding, and ejected particles

6 within each time period of 10^{-4} s, where $u_* = 0.5 \text{ m s}^{-1}$, $d_m = 228 \mu\text{m}$, and $\sigma_p = \exp(0.3)$.

7 (b) Comparison of the simulated total mass flux with the most commonly-used

8 semiempirical saltation mass flux equations (Bagnold, 1941; Kawamura, 1951; Lettau

9 and Lettau, 1978; Owen, 1964; Sørensen, 2004), where $d_m = 228 \mu\text{m}$, and $\sigma_p = \exp$

10 (0.3). (c) Comparison of the simulated charge-to-mass ratio distribution in the range

11 of 0.07-0.09 m height with the measured mean charge-to-mass ratio, in the range of

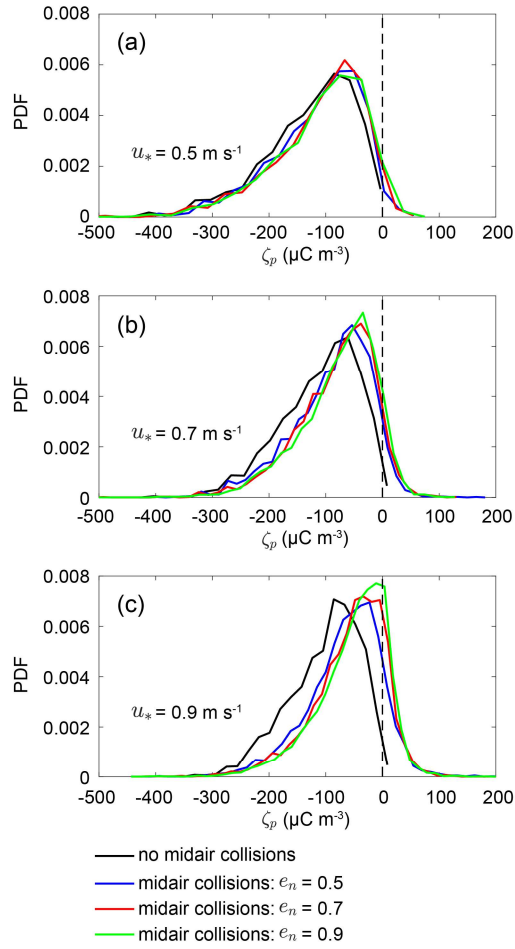
12 0.06-0.1 m height (Zheng et al., 2003), at 0.05 m height (Schmidt et al., 1998) and 0.08

13 m height (Bo et al., 2014). Here, $\rho_h^0 = 6 \times 10^{15} \text{ m}^{-2}$ is determined by calibrating the model14 with measurements; $u_* = 0.35 \text{ m s}^{-1}$, $d_m = 203 \mu\text{m}$, and $\sigma_p = \exp(0.33)$ are estimated

15 from (Zheng et al., 2003).

16

1

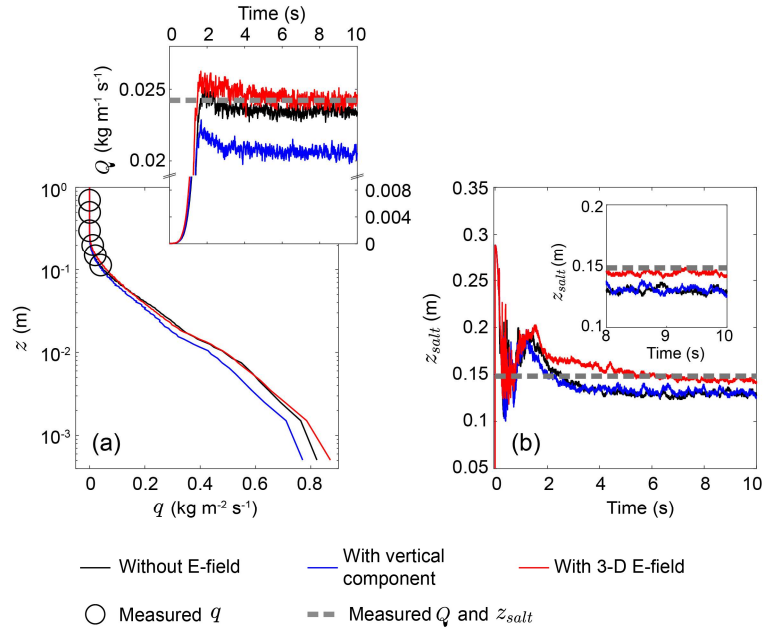


2

3 **Figure 7.** Effects of midair collisions on the probability density function (PDF) of charge-
4 to-mass ratio of saltating particles for various wind velocities (a) $u_* = 0.5 \text{ m s}^{-1}$, (b)
5 $u_* = 0.7 \text{ m s}^{-1}$, and (c) $u_* = 0.9 \text{ m s}^{-1}$, where $d_m = 203 \text{ }\mu\text{m}$, $\sigma_p = \exp(0.33)$, and $\rho_h^0 = 6 \times 10^{15}$
6 m^{-2} .

7

1

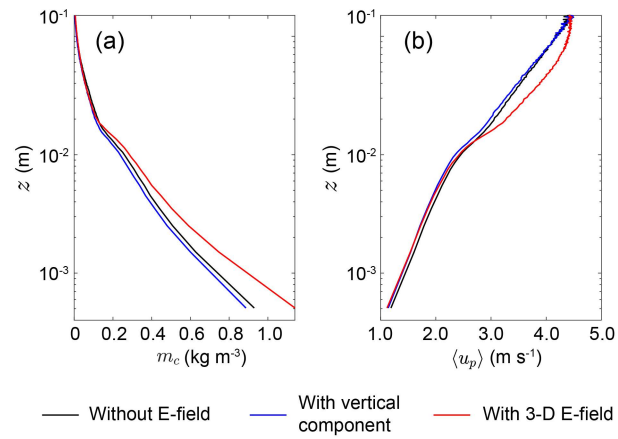


2

3 **Figure 8.** Comparison of the simulated mass flux q and total mass flux Q (a) and
 4 saltation height z_{salt} (b) with our measurements in the relatively steady period of the
 5 observed dust storm (shaded in Fig. 4 and Fig. S3 in the Supplement), where $u_* = 0.37$
 6 m s⁻¹, $d_m = 200 \mu\text{m}$, $\sigma_p = \exp(0.42)$, $\rho_h^0 = 6 \times 10^{15} \text{ m}^{-2}$, and $e_n = 0.7$. (a) Circles are the
 7 measured mean mass flux, dashed line denotes the estimated mean total mass flux,
 8 and lines denote the simulated results. (b) Dashed lines denote the estimated saltation
 9 height based on our measurements and lines denote simulated results. The
 10 uncertainty analysis of the measured or estimated results can be found in Text S1 in
 11 the Supplement.

12

1



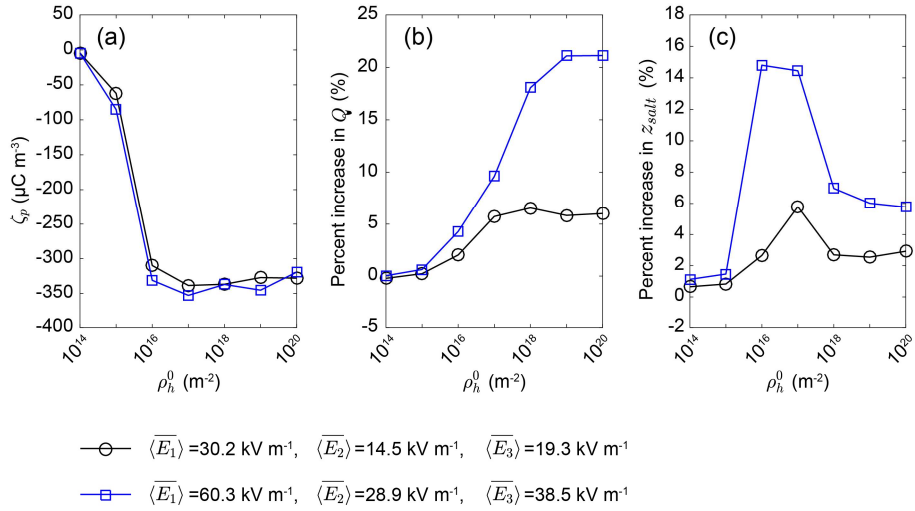
2

3 **Figure 9.** Vertical profiles of the particle mass concentration m_c and mean particle

4 horizontal speed $\langle u_p \rangle$ for different cases, where $u_* = 0.37 \text{ m s}^{-1}$, $d_m = 200 \text{ }\mu\text{m}$,

5 $\sigma_p = \exp(0.42)$, $\rho_h^0 = 6 \times 10^{15} \text{ m}^{-2}$, and $e_n = 0.7$.

6



2

3 **Figure 10.** Effects of the density of charged species ρ_h^0 on saltation for two different
4 height-averaged time-varying mean levels (i.e. $\langle \bar{E}_i \rangle$, $i = 1,2,3$). (a) The mean charge-
5 to-mass ratio ζ_p (in the range from 0.07 to 0.09 m height) as a function of ρ_h^0 ranging
6 from 10^{14} to 10^{20} m⁻² (e.g. Kok and Lacks, 2009). (b) Percent increase in the total mass
7 flux Q as a function of ρ_h^0 . (c) Percent increase in the saltation height z_{salt} as a
8 function of ρ_h^0 . The squares correspond to the height-averaged time-varying mean in
9 the steady stage of the observed dust storm (shaded in Fig. S7 in the Supplement). In
10 these cases, $e_n=0.7$.

Supplement of

Effects of three-dimensional electric field on saltation during dust storms: An observational and numerical study

Huan Zhang¹, You-He Zhou^{1*}

¹Department of Mechanics and Engineering Science, College of Civil Engineering and Mechanics, Lanzhou University, Key Laboratory of Mechanics on Disaster and Environment in Western China, The Ministry of Education of China, Lanzhou 730000, PR China.

Contents of this file

- Text S1 to S2
- Figs. S1 to S8

Additional Supplement (File uploaded separately)

- Caption for Dataset S1

Introduction

Text S1 describes the estimations of the size distribution of the saltating particles, saltation mass flux, and saltation height based on the SPC-91 data. Text S2 describes the measurement uncertainties of the VREFM sensor. The E-field data measured in our field campaign are provided as a CSV file in Dataset S1. Additional figures (i.e., Figs. S1-S8) that support the findings of this study are also included.

*Corresponding author: You-He Zhou, zhouyh@lzu.edu.cn

Text S1. Estimating the size distribution of the saltating particles, saltation mass flux, and saltation height based on the SPC-91 data

Because SPC-91 sensors measure particle number passing through the measurement area ($L_x=2$ mm in height and $L_y=25$ mm in length) per second in the range of 30-490 μm with 64 bins, the probability distribution function (PDF) of the saltating particle size can be readily estimated by

$$f(d < d_i < d + \Delta d) = \frac{N_i}{\Delta d \sum_{i=1}^n N_i} \quad (\text{s1})$$

where $f(d < d_i < d + \Delta d)$ denotes the probability density of particle size in the range of $(d, d + \Delta d)$; N_i and d_i are the number and diameter of the i -th particle bin, respectively. Examples of the PDF of the saltating particle size are shown in Fig. S1. It can be seen that the size of saltating particles at different heights nearly obeys a log-normal distribution (with R^2 of 0.85-0.96).

In our field campaign, we measured the saltating particle number flux at 6 heights from 0.05 to 0.7 m. Thus, the mass flux at each measurement height can be reasonably estimated by

$$q(z) = \frac{\pi \rho_p}{6L_x L_y T_w} \sum_{i=1}^n (N_i d_i^3) \quad (\text{s2})$$

Note that the summation \sum is performed for the particles located in the range of $[z, z + \Delta z]$ over the 30-min time windows (i.e., $T_w=30$ minutes), in order to collect sufficient sand samples and capture the full range of turbulent fluctuations (e.g. Martin and Kok, 2017; Sherman and Li, 2012). Since SPC-91 measures the particle diameter with an uncertainty of $\Delta d = \pm 0.015$ mm (see SPC-91 Installation Guide, Niigata Electric Co., Ltd. for details), the uncertainty of estimating mass flux is $\Delta q \sim 3d^2\Delta d$ (i.e. $q \sim d^3 \Rightarrow \Delta q \sim 3d^2\Delta d$). As shown in Fig. S2, the measured mass flux data during different time intervals can be well fitted by the exponential functions

(Shao, 2008):

$$q(z) = q_0 \exp(-az) \quad (s3)$$

where q_0 is the value of q at $z = 0$ and a is a positive empirical constant. Hence, the total mass flux can be determined by

$$Q = \int_0^{+\infty} q(z) dz = \frac{q_0}{a} \quad (s4)$$

Similarly, the uncertainty of the total mass flux is

$$\Delta Q = \frac{a\Delta q_0 - q_0\Delta a}{a^2} \quad (s5)$$

Additionally, the saltation height, which is defined as the height below which 99 % of the total mass flux is present, can be given by (Dupont et al., 2013; Kok et al., 2012)

$$\int_0^{z_{salt}} q(z) dz = \frac{0.99q_0}{a} \quad (s6a)$$

$$\Rightarrow z_{salt} = -\frac{\ln(0.01)}{a} \quad (s6b)$$

Similarly, the uncertainty of the saltation height is

$$\Delta z_{salt} = -\frac{\ln(0.01)}{a^2} \Delta a \quad (s7)$$

As shown in Fig. S3, the estimated saltation height slightly varies with time, and thus we use the mean saltation height, which is 0.172 ± 0.0343 m, to obtain the dimensionless height z^+ . For different time windows (i.e. $T_w = 5, 10, 30$ minutes),

there is no obvious differences between the mean values of Q and z_{salt} , but the standard deviations decrease as T_w increases (Fig. S3).

Text S2. Measurement uncertainties of VREFM sensor

Fig. S4 shows the calibration results of three representative VREFM sensors. It can be seen that there is an excellent linear relationship ($R^2=0.99-1$) between the output voltage of VREFM and the applied E-field intensities. The uncertainties of the VREFM sensor come primarily from the fluctuation of the output voltage of VREFM sensors under a constant applied E-field, as shown in the left panels of Fig. S4. The uncertainties of a VREFM sensor under specific applied E-field can be defined as

$$\frac{k_{V-E}V'_{max}}{E_{applied}} \times 100\% \quad (s8)$$

where k_{V-E} is the slope of the fitting line in the right panels of Fig. S4; V'_{max} is the maximum fluctuation of the output voltage of VREFM sensors; and $E_{applied}$ is the applied E-field intensity in the parallel-plate E-field calibrator. From the calibration results, we found that the maximum uncertainties of VREFM ranged from $\sim 1.38\%$ to $\sim 2.24\%$.

Dataset S1. (ds01.csv) A CSV file contains 3-D E-field data measured in our field campaign from 13:00 to 19:00 on May 6, 2014, at the QLOA site. E1(1) to E1(5) represent the streamwise E-field at 0.05 to 0.7 m height, respectively; E2(1) to E2(5) represent the spanwise E-field at 0.05 to 0.7 m height, respectively; and E3(1) to E3(5) represent the vertical E-field at 0.05 to 0.7 m height, respectively. All data in the CSV file are shown in kV m^{-1} .

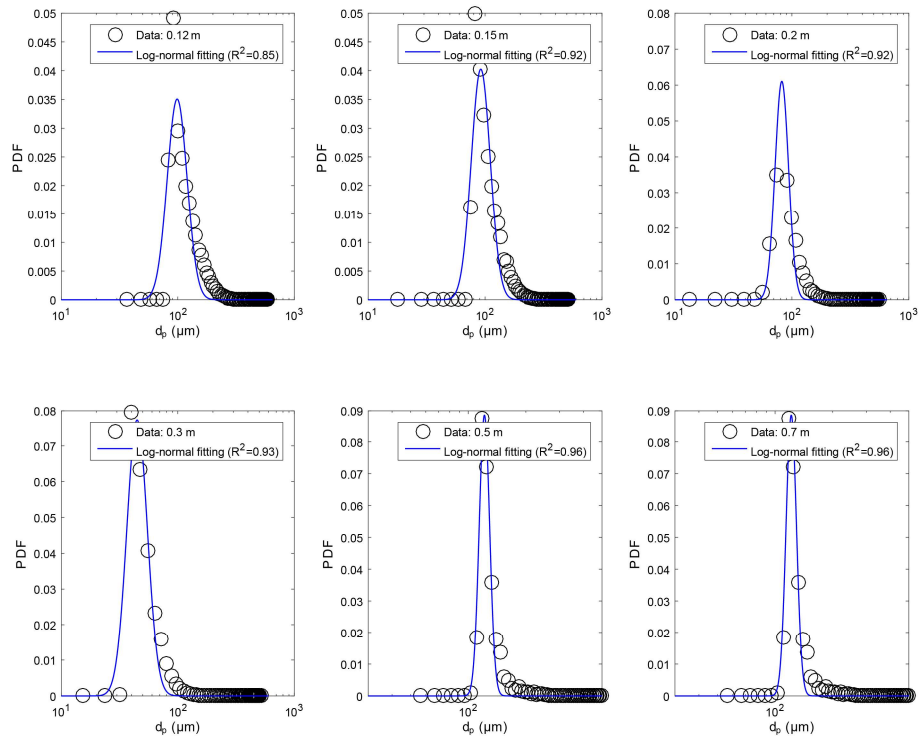


Figure S1. PDFs of the saltating particle size at different heights in the relatively stationary period of the observed dust storm (shown as the shaded area in Fig. 4 of the manuscript). Open squares denote measured data by SPC-91 sensors, and lines denote log-normal (i.e. Eq. 9 in the manuscript) fitting.

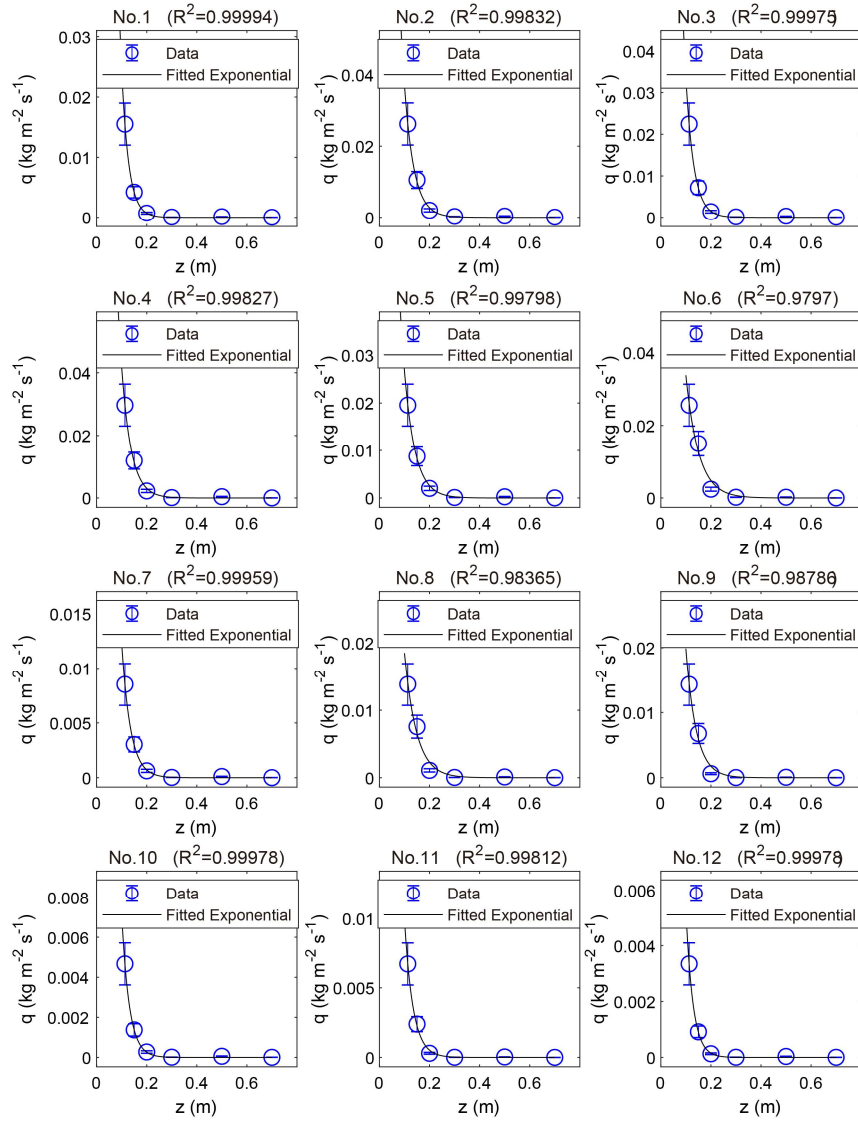


Figure S2. An example of the estimation of the total mass flux Q and saltation height z_{salt} in this study, where No. i corresponds to time interval of $[(i - 1)T, iT]$. The measured mass flux data are fitted by the exponential function $q(z) = q_0 \exp(-az)$, with R^2 larger than 0.9. Thus, the total mass flux and saltation height can be estimated by Eqs. s4-s7 in the Supplement, respectively.

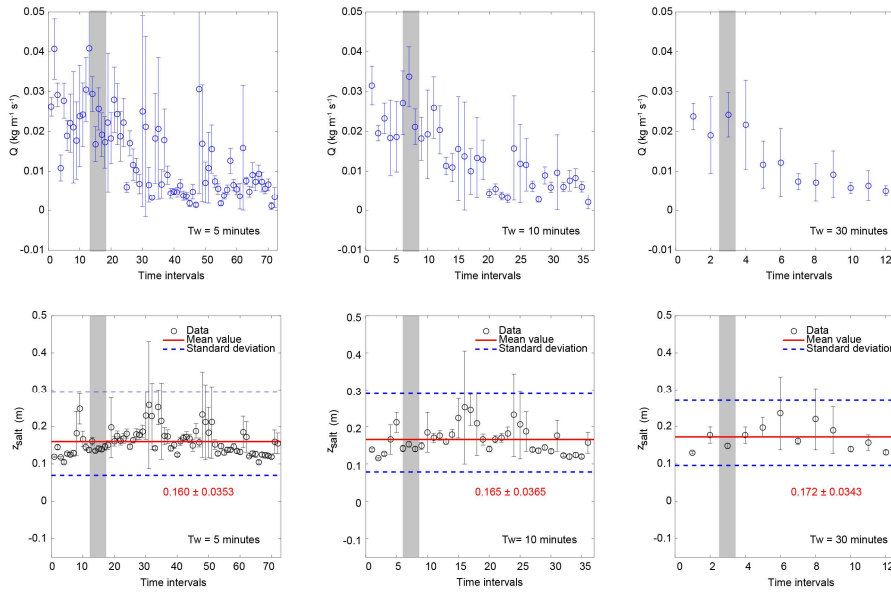


Figure S3. The estimated total mass flux Q (upper panels) and the saltation height z_{salt} (lower panels) with different time windows T_w (i.e. 5, 10, and 30 minutes) using the methods described in the Text S1. In the lower panels, the horizontal lines (in red) denote the mean saltation height, and the horizontal dashed lines (in blue) denote standard deviation. The shaded areas denote the relatively steady period of the observed dust storm.

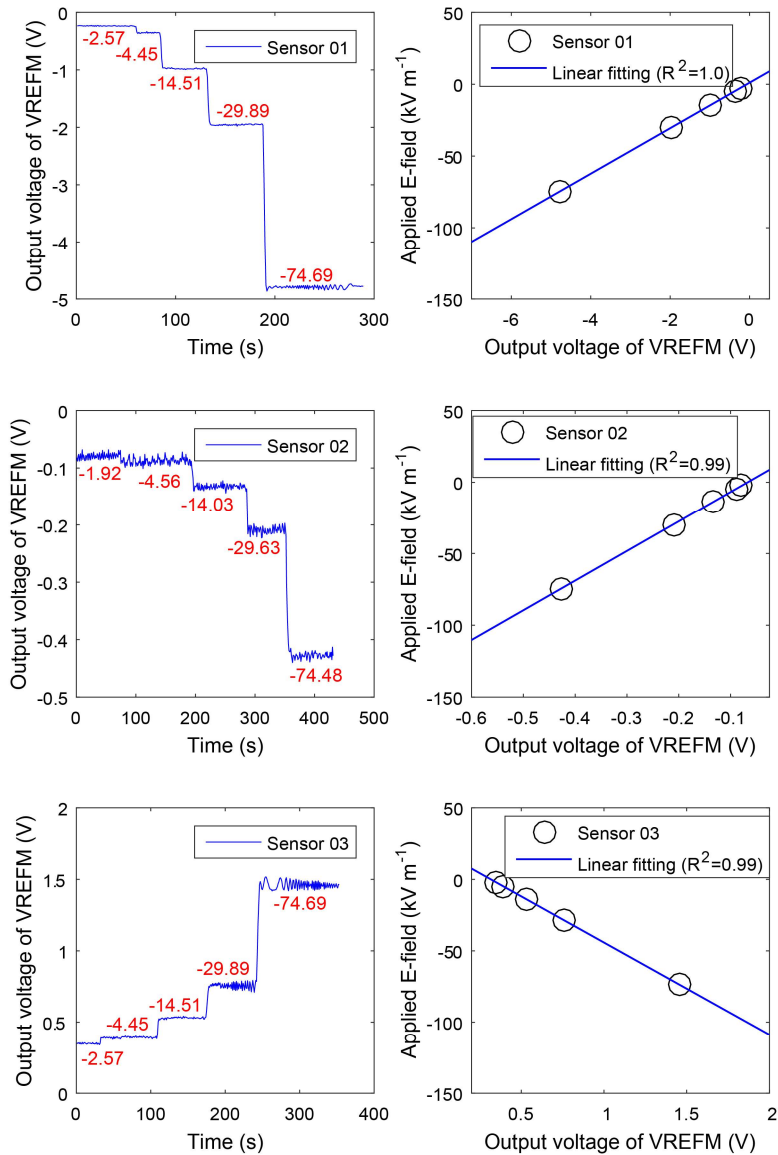


Figure S4. Examples of the calibration curves between the output voltage of the VREFM sensor and the applied E-field in the parallel-plate calibrator. The left panels are time series of the output voltage of the VREFM sensor at five different applied E-field levels (from $\sim 2 \text{ kV m}^{-1}$ to $\sim 75 \text{ kV m}^{-1}$ labeled in red). The right panels are the significant linear relationships between the output voltage of VREFM and the applied E-field intensity.

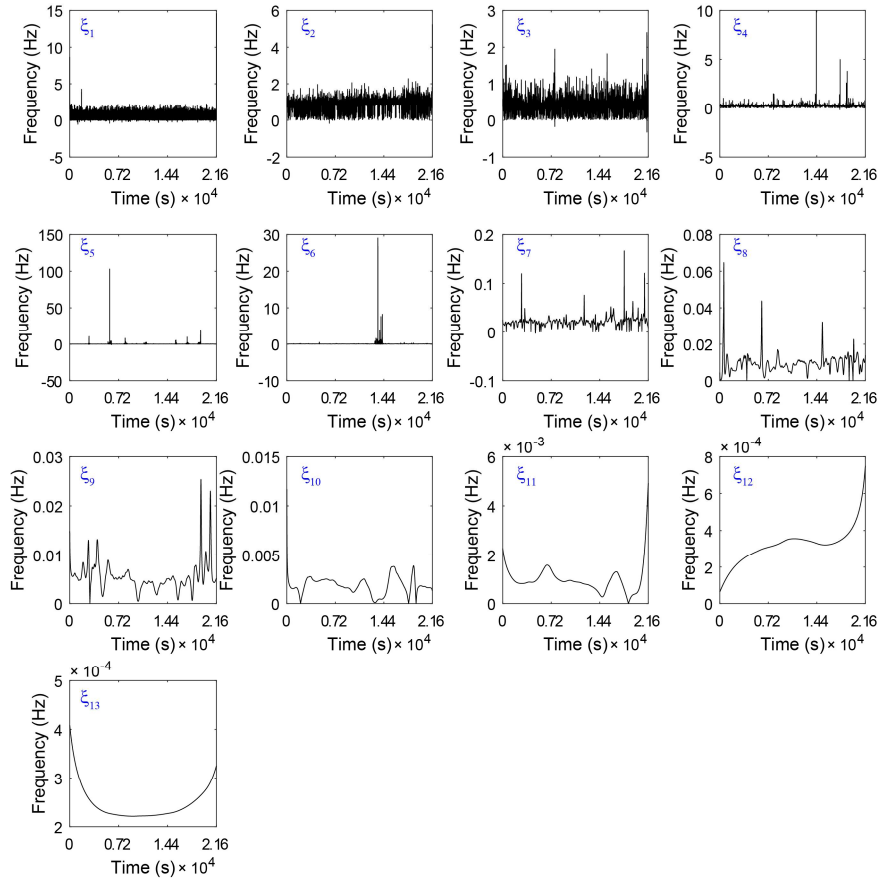


Figure S5. The instantaneous frequency of the EEMD components ξ_1 - ξ_{13} for the vertical E-field series at 0.5 m height, i.e. $E_3(0.5)$.

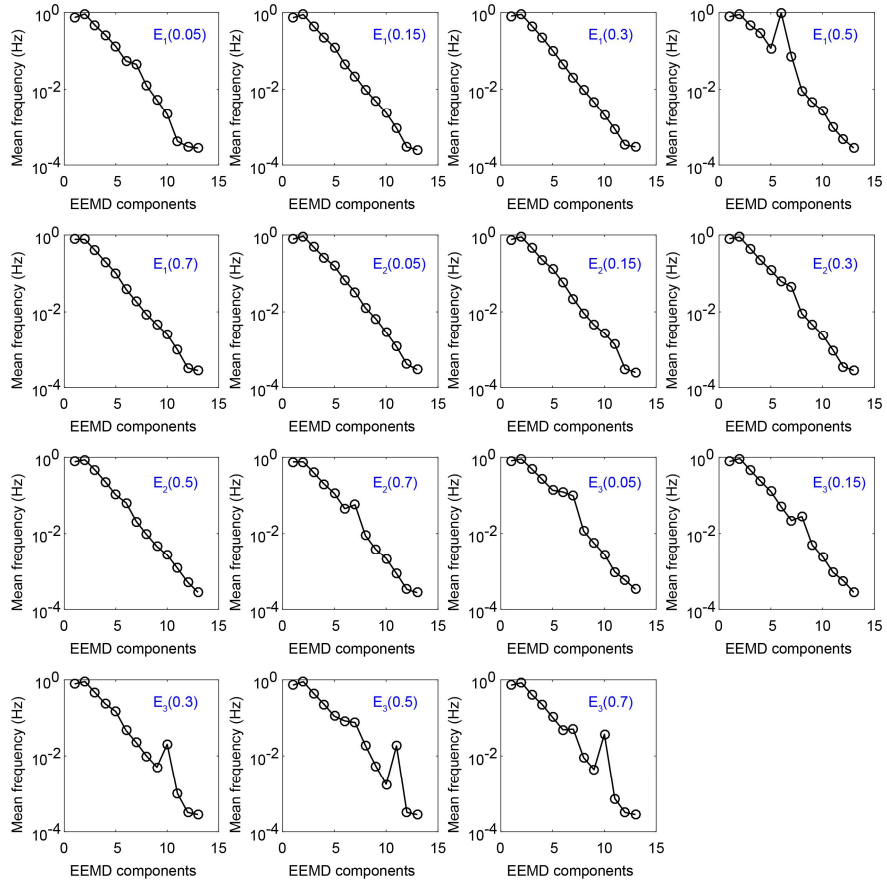


Figure S6. The mean frequencies of the EEMD components ξ_1 - ξ_{13} for the total of 15 components of the observed 3-D E-fields, i.e. E_1 - E_3 from 0.05 to 0.7 m height.

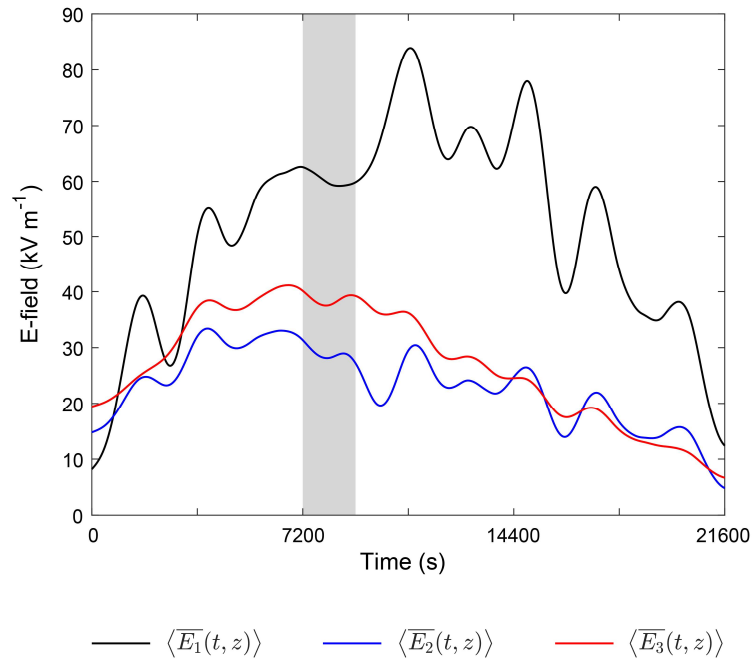


Figure S7. The height time-varying mean series of the 3-D E-field. The shaded area denotes the relatively steady period of the observed dust storms. Times are shown relative to May 6, 2014 at 13:00:00 UTC+8.

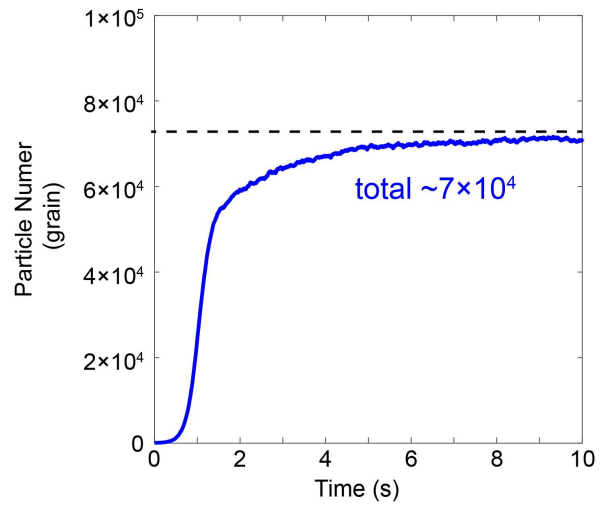


Figure S8. The total number of saltating particles in the case of Fig. 6 in the manuscript.

References

- Dupont, S., Bergametti, G., Marticorena, B., and Simoens, S.: Modeling saltation intermittency, *J. Geophys. Res.-Atmos.*, 118, 7109–7128, doi:10.1002/jgrd.50528, 2013.
- Kok, J. F., Parteli, E. J., Michaels, T. I., and Karam, D. B.: The physics of wind-blown sand and dust, *Rep. Prog. Phys.*, 75, 106901, doi:10.1088/0034-4885/75/10/106901, 2012.
- [Martin, R. L., and Kok, J. F.: Wind-invariant saltation heights imply linear scaling of aeolian saltation flux with shear stress, *Sci. adv.*, 3, doi: 10.1126/sciadv.1602569, 2017.](#)
- Shao, Y. P.: *Physics and Modelling of Wind Erosion*, Springer Science & Business Media, Heidelberg, 2008.
- [Sherman, D. J., and Li, B.: Predicting aeolian sand transport rates: A reevaluation of models, *Aeolian Res.*, 3, 371-378, doi: 10.1016/j.aeolia.2011.06.002, 2012.](#)